JOURNAL OF AIRCRAFT
Vol. 59, No. 4, July–August 2022

Effect of Turbulence Modeling Selection Within Helios for Small Quadrotor Aerodynamics

Austin D. Thai* and Sheryl M. Grace†
Boston University, Boston, Massachusetts 02215
and
Rohit Jain‡
U.S. Army Combat Capabilities Development Command, Aviation & Missile Center, Moffett Field, California 94035

https://doi.org/10.2514/1.C036410

The high-fidelity rotorcraft simulation framework HPCMP CREATE-AV Helios was used to study the impact of turbulence modeling methods on the prediction of a small quadrotor unmanned aerial vehicle. First, the vehicle's rotor was simulated as an isolated rotor in both hover and forward flight for turbulence model assessment. Predictions using a fully turbulent turbulence model were compared with predictions from several laminar–turbulent transition models. Both comparison with experiments and computational performance were considered. The laminar–turbulent transition models predicted flow separation near the tip for all flight conditions simulated, leading to lower torque and thrust than the fully turbulent model, which predicted attached turbulent flow. The fully turbulent model was shown to provide reasonable comparison with experiments with the lowest computational cost and was used for full vehicle simulations. The full quadrotor configuration calculations were performed in hover and forward flight. The forward flight simulations were performed with and without a detached eddy simulation method, and similar interactional aerodynamics were predicted. The Helios simulation suite is shown to be well-suited for prediction of aerodynamic performance of small-scale rotorcraft.

Nomenclature

A	=	rotor area, m^2
C_Q	=	coefficient of torque, $Q/(\rho\pi R^5\Omega^2)$
C_T	=	coefficient of thrust, $T/(\rho\pi R^4\Omega^2)$
c	=	mean rotor chord, m
F	=	force, N
FM	=	figure of merit
$f_{\text{threshold}}$	=	adaptation threshold function
M	=	moment, N · m
p	=	static surface pressure, Pa
p_∞	=	atmospheric pressure, Pa
Q	=	torque, N · m
q	=	q-criterion, s^{-2}
R	=	rotor radius, m
r	=	rotor spanwise coordinate, m
S	=	strain rate tensor, s^{-1}
T	=	thrust, N
y^+	=	dimensionless wall spacing
Γ	=	rotation rate tensor, s^{-1}
ρ	=	air density, kg/m^3
τ	=	wall shear stress, Pa
Ω	=	rotor rotation speed, rad/s

Subscripts

x	=	x component
y	=	y component
z	=	z component

Received 4 February 2021; revision received 2 November 2021; accepted for publication 2 December 2021; published online 10 January 2022.

*Graduate Research Assistant, Department of Mechanical Engineering; adthai@bu.edu. Student Member AIAA.

†Associate Professor, Department of Mechanical Engineering; sgrace@bu.edu. Associate Fellow AIAA.

‡Aerospace Engineer. Senior Member AIAA.

I. Introduction

THE unmanned aerial vehicle (UAV) market is dominated by rotorcraft due to their vertical takeoff and landing (VTOL) capabilities. As more of these aircraft are produced to fulfill demands for commercial package delivery, aerial photography, and search-and-rescue, computational fluid dynamics (CFD) methods that can predict their aerodynamics must be understood and validated. These high-fidelity numerical tools can be used to improve the performance, safety, and operation of next-generation designs. The software chosen for use in this investigation is the rotorcraft simulation suite High Performance Computing Modernization Program (HPCMP) CREATE-AV™ Helios version 10.1, maintained by the U.S. Army Combat Capabilities Development Command Aviation & Missile Center (DEVCOM AvMC) [1–3]. Helios is an overset CFD solver that allows the user to select one of four solvers for the rotor and fuselage near-body regions that are then coupled to an off-body Cartesian-grid solver.

Similar to many popular CFD solvers for rotorcraft simulations, Helios implements unsteady Reynolds-averaged Navier–Stokes (RANS), in which the turbulent part of the flow is separated via Reynolds decomposition. A turbulence model accounts for the Reynolds stresses. Although many turbulence models have been developed, the popular ones used for helicopter simulations are fully turbulent, which is a valid assumption because large helicopters operate at large Reynolds numbers, on the order of 10^7, where the flow is predominantly turbulent. A literature survey on turbulence modeling for rotor performance predictions suggests that this topic is an area of active research. For example, a special section on the simulation of rotorcraft in hover from the *Journal of Aircraft* described computations of the S-76 rotor that showed that fully turbulent models are able to obtain very good agreement with experimental data [4–6]. While some find good agreement using fully turbulent models, others have added a transition model that accounts for laminar–turbulent transition and found an improvement in the rotor figure of merit [7–9].

Small rotors of a UAV operate at Reynolds numbers on the order of 10^5 where laminar–turbulent transition should play an even more important role than for large rotorcraft. Because of their increasing popularity, it is easy to find published research related to both UAV design and performance [10–13]. However, there has not been an

intensive research study dedicated to validating CFD methods for these smaller rotorcraft. Most CFD studies of UAVs assume fully turbulent flow, such as those of Thai et al. [14] and Lakshminarayan and Baeder [15], who both show good thrust prediction but imperfect torque prediction. Other researchers used fully turbulent models but did not report the torque or provide comparisons to experimental data. For example, Diaz and Yoon simulated various commercially available multirotor UAVs and discussed design modifications to improve their efficiency in forward flight [16]. However, the torque calculation was not validated, and therefore efficiency claims could be misguided. Similarly, both Hwang et al. [17] and Misiorowski et al. [18] attempted to predict the influence of aerodynamic interactions on quadrotor performance using CFD without discussion of the validation of the method or the selection of a turbulence model. Zawodny and Boyd Jr. [19] were able to capture the acoustics of the interaction between a small rotor and a representative airframe but did not reveal the turbulence model that was used. More recent studies by Ranjan et al. and Lopes et al. investigated advanced turbulence modeling at low Reynolds number focusing mostly on simplified airfoil and wing configurations rather than rotors [20,21].

The main objective of the research reported in this paper is to investigate the effect of different turbulence models in mStrand, which has been selected as the Helios near-body solver, and SAMCart, the default off-body solver, on performance predictions of small rotorcraft. In addition, we extend the simulation envelope to forward flight conditions, which has not received much attention [14,22–25]. The analysis includes airload distributions that may hold clues to understanding best practices for such simulations. Finally, we discuss the balance between any accuracy benefit from including the additional transition equations and the increase in computational time which for Helios simulations has previously been reported as up to a 50% increase [26].

The Methods section provides introduction to the numerical solver and transition models available in Helios (Sec. II.A). The fuselage and rotor geometry, including the source of the Computer-Aided Design (CAD) surfaces, used for this study are described in Sec. II.B. A discussion of the computational mesh follows in Sec. II.C including grid convergence results. Several other simulation settings are briefly mentioned in Sec. II.D. Section III.A presents the results for the isolated rotor in hover at various revolutions per minute (RPMs) simulated with a fully turbulent and three laminar–turbulent transition models. A single transition model and the fully turbulent model were used to simulate a single rotor in forward flight, and the results are shown in Sec. III.B. Finally, Sec. IV describes the predictions of the full quadrotor using the fully turbulent stress model with the addition of DES.

II. Methodology

A. Numerical Solver and Transition Models

The near-body solver used for this study is mStrand, a second-order finite volume code that automatically generates the near-body strand-based volume mesh given a surface mesh. More information on strand grids can be found in [27–30]. Further details of the mStrand solver, such as discretization schemes, can be found in Ref. [31]. The off-body solver in Helios is SAMCart [32]. SAMCart uses a fifth-order central difference scheme with fourth-order viscous terms. The near-body solvers are body-fitted to better capture the complex geometries, and the resultant flow is then passed onto the higher order off-body solver that limits numerical dissipation. SAMCart enables adaptive mesh refinement (AMR) to resolve important flow structures such as the vortices that are generated by a rotor and propagate into its wake.

The Spalart–Allmaras (SA) turbulence model was selected for this study due to its popularity, accuracy, robustness, and computational efficiency [33]. This model assumes that the flow is fully turbulent everywhere. For low-Reynolds-number flows, representative of small multirotors, additional equations may be added to a fully turbulent model to account for laminar–turbulent transition. The transition models available in Helios that are compatible with SA are the two-equation local-correlation-based Medida–Baeder (MB) model [34], the updated one-equation local-correlation-based model (M15) developed by Menter et al. [35], and the linear-stability-theory-based Amplification Factor Transport (AFT) 2017b model developed by Coder and associates [36–38].

The MB model is a two-equation model that introduces the transport equations for intermittency and momentum thickness Reynolds number from the Langtry–Menter transition model [39] into the SA model. The production and destruction terms in the SA model are multiplied by a function of the intermittency to further control the eddy viscosity [34]. The M15 model is a one-equation model that uses the intermittency transport equation of the Langtry–Menter model but avoids the momentum thickness Reynolds number equation by instead adding correlations for the critical Reynolds number. In mStrand, the M15 model is coupled to the SA model via the same intermittency relationship as the MB model [34]. The 2017b version of the AFT model solves one equation for the amplification factor and one equation for the natural logarithm of the intermittency. The AFT model is coupled to the SA model through a modification of the eddy-viscosity transport equation using the intermittency. However, unlike the correlation-based models, only one of the functions that appear in both the production and destruction terms is modified. Readers are referred to the original papers by the authors of the transition models for more details. The fully turbulent SA model and its coupling to the three transition models, SA-M15, SA-AFT, and SA-MB, are each evaluated in this paper for accuracy and performance.

B. SUI Endurance

The SUI Endurance is a commercially available quadrotor drone that was designed by Straight Up Imaging (SUI) for aerial photography. The rotor used on the aircraft is Tiger Motor's T-Motor P15x5, referred to in this paper as the T-Motor rotor. The fuselage was designed in-house at SUI. Availability of experimental data for validation motivated the selection of the SUI. The Rotorcraft Aeromechanics branch at NASA Ames [40,41] tested the T-Motor rotor in isolation in both hover and forward flight. The full SUI Endurance vehicle was also tested in both hover and forward flight. The fuselage geometry used in the current paper is a CAD model generated by SUI obtained by the Rotorcraft Aeromechanics branch during the NASA study. The motor shafts, which would be hidden during installation of the rotor, were removed from the CFD model, shown in Fig. 1. The T-Motor rotor geometry, which is a twin-bladed rotor with a radius of $R = 0.1905$ m, was provided as both a CAD model and as airfoil coordinates together with sectional properties. Both the CAD model and the airfoil coordinates were derived from laser scans performed for the NASA study. The rotor geometries had several discrepancies and physical irregularities that were attributed to low laser scanning resolution. Therefore, the blade geometry used for simulations in this paper, shown in Fig. 2, was derived from a combination of the airfoil coordinates and CAD model. The airfoil coordinates were provided with a blunt trailing edge and were rounded using tangent splines for the simulations in this paper. The derived blade sectional properties are plotted against the original laser scanned sectional properties in Fig. 3. The mean chord is $c = 0.0296$ m and the twist at 75% span is 9.59 deg.

C. Simulation Setup

The simulations were run with unsteady RANS in both the near-body and off-body with a time step corresponding to 0.25 deg azimuth. The full quadrotor forward flight configurations have differing rotor speeds, and the 0.25 deg azimuth time step corresponds to the slowest rotor. The adaptive mesh refinement capability used in this paper is dependent on a threshold function, $f_{\text{threshold}}$, proposed by Kamkar et al. [42]. This threshold function is a normalization of the q-criterion, q, by the strain rate tensor:

$$f_{\text{threshold}} = \frac{q}{\|S\|^2} = \frac{1}{2}\left(\frac{\|\Gamma\|^2}{\|S\|^2} - 1\right) \tag{1}$$

Regions of the domain are refined where $f_{\text{threshold}}$ was greater than 1. This approach was first proposed by Kamkar et al. [42] and has been

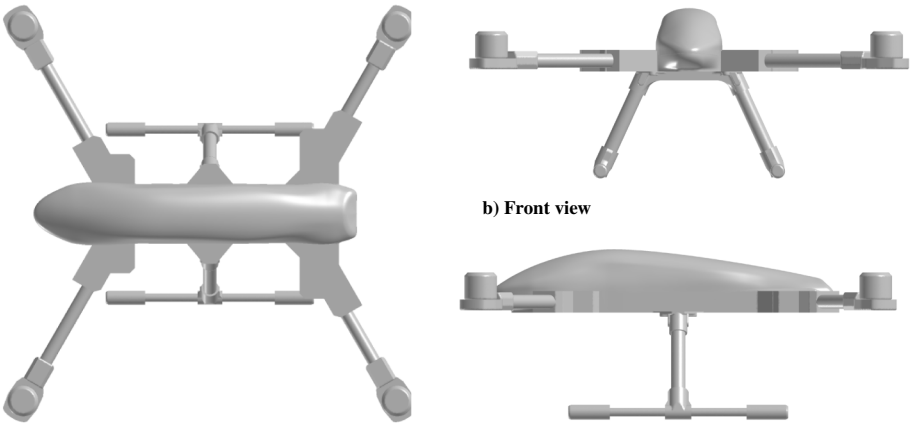

a) Top view b) Front view c) Side view

Fig. 1 Various views of the simulated fuselage geometry for the SUI Endurance quadrotor.

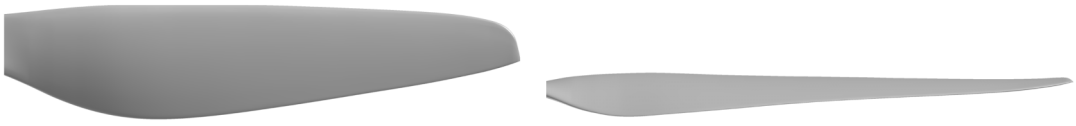

a) Suction side view b) Trailing edge view

Fig. 2 Simulated counterclockwise T-Motor blade geometry.

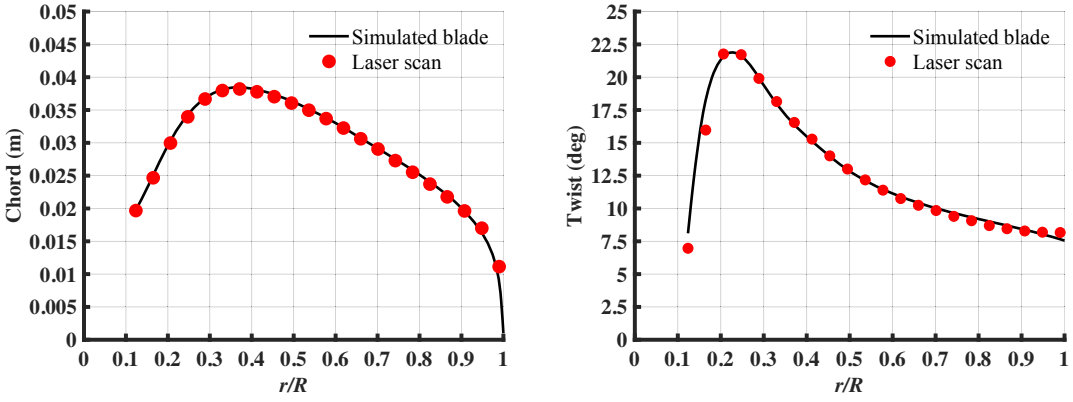

Fig. 3 Chord and twist for the derived blade geometry versus the laser scanned properties by Russell et al. [40,41].

used across many rotorcraft applications of different scales. In isolated rotor studies, AMR is activated in the far field after the first two revolutions to allow transient effects to dissipate. In the full quadrotor studies, AMR is activated after the first revolution of the slowest rotor.

The freestream turbulence intensity was set to the default setting in mStrand (0.08165%), which is reasonable for the Army 7×10 Wind Tunnel at the flow speeds used in the experiments [40,41]. The wind tunnel walls, which may induce recirculation effects, were not considered in this computational study.

For reference, all of the isolated rotor in hover cases were run on 480 cores on the Department of Defense Supercomputing Resource Center (DSRC) Onyx (2.8 GHz Intel Broadwell E5-2699v4), excluding the 3500 RPM case run with the SA model, which was run on 440 cores on the DSRC Gordon (2.3 GHz Intel Xeon E5-2698v3). All of the isolated rotors in forward flight cases were run on 440 cores on Onyx. The full quadrotor cases were run with 1584 cores on Onyx.

D. Computational Mesh

1. *Near-Body Mesh*

The near-body surface mesh for the rotor blades is generated automatically at runtime by mStrand's bladeGen, which automatically generates the blade geometry via specification of airfoil coordinate files and sectional properties (twist, chord length, and quarter-chord positions). The near-body volume mesh was also generated automatically. The distance of the strand, which corresponds to the height from the surface, was set to $0.4c$. This corresponds to the default setting in mStrand and is in the range of acceptable strand lengths as previously reported by Lakshminarayan et al. [43]. The total number of normal points was initially set to 51, and the wall spacing, $1.45 \times 10^{-4}c$, was computed to ensure $y^+ < 1$ based on the tip speed at 3500 RPM.

An initial study into the effect of transition modeling in mStrand by Tran et al. was used as a guide for the current grid study [26]. Tran et al. simulated the S809 airfoil in 2D at various angles of attack with increasing number of points around the airfoil ranging from 327 to 1127 in increments of 200. The cases were run at a Reynolds number of 2×10^6, which is much larger than the magnitude range of 10^5 experienced by the rotor simulated in this paper. In summary, Tran et al. showed that the standard SA model and the SA-MB model had low grid dependence, with only 4% difference in drag coefficient from coarsest to finest grids. However, the SA-AFT model was heavily grid dependent, with drag coefficient differences up to 36% from coarsest to finest grid resolution. The SA-AFT model did not appear to converge even from 727 to 1127 points, still changing by up to 21%. The lift coefficient across all models was fairly grid independent varying at most by 5% from coarsest to finest.

Table 1 Results of grid study

	C_T, 10^{-3}		C_Q, 10^{-4}	
Points (airfoil × span)	SA	SA-AFT	SA	SA-AFT
100 × 220	9.174 (— —)	8.605 (— —)	9.975 (— —)	9.427 (— —)
150 × 220	9.159 (−0.16)	8.618 (+0.15)	9.685 (−2.90)	9.182 (−2.60)
200 × 220	9.194 (+0.39)	8.758 (+1.62)	9.674 (−0.11)	9.306 (+1.35)
250 × 220	9.231 (+0.40)	8.880 (+1.39)	9.695 (+0.21)	9.431 (+1.35)
350 × 220	9.247 (+0.18)	8.979 (+1.12)	9.699 (+0.05)	9.552 (+1.28)
200 × 160	9.196 (— —)	8.745 (— —)	9.674 (— —)	9.317 (— —)
200 × 190	9.194 (−0.03)	8.748 (+0.04)	9.671 (−0.03)	9.300 (−0.18)
200 × 220	9.194 (+0.00)	8.758 (+0.12)	9.674 (+0.03)	9.306 (+0.06)
Experiment	9.323		9.322	

Percent change with refinement is reported in parentheses.

The large number of grid points used in the airfoil study by Tran et al. is not feasible or practical for full 3D CFD simulations of rotors. In fact, Tran et al. simulated a rotor blade in 3D with 300 points around the airfoil, which is even less than the coarsest airfoil mesh in the 2D simulations [26]. In addition, Tran et al. did not include a 3D rotor blade grid study. We address this gap here by evaluating the grid dependence properties of the fully turbulent model and a transition model to determine the impact on 3D rotor performance prediction. Because Tran et al. showed SA-AFT has the strictest convergence properties [26], it was the transition model used for the grid study in the current work.

The bladeGen framework enables simple mesh modification during the automatic generation process via specification of leading and trailing edge spacing, root and tip spacing, and the number of spanwise points and points around the airfoil. The T-Motor rotor blade was generated using bladeGen within the mStrand solver. The laser scanned airfoil closest to the hub was at $r/R = 0.1237$. No extrapolation was performed to extend the computational geometry to smaller radii to match the physical rotor. Therefore, the forces that are generated by the rotor portion nearest the hub are neglected. The effects are expected to be small due to the low relative velocity in this region. The leading and trailing edge spacings were kept constant at $5.8 \times 10^{-4}c$, the root spacing was set to $5.8 \times 10^{-4}c$, and the tip spacing was set to $1.2 \times 10^{-4}c$. The number of chordwise points around a section was varied from 100 to 350, while keeping the number of points along the span at 220. The upper and lower surfaces of the rotor blades were always set to have equal numbers of points.

To evaluate the effect of grid spacing on the rotor blades, the T-Motor rotor was simulated at the nominal 3500 RPM. At this RPM, the Reynolds number range across the blade sections is in the range of 10^5 and the rotor has a tip speed of 0.205 Mach. The rotor was simulated for 10 rotor revolutions, which is more than sufficient for temporal convergence. The thrust coefficient C_T and torque coefficient C_Q results are given in Table 1.

The points are reported as (points around airfoil × spanwise points). To emphasize the two refinement studies the upper section of Table 1 corresponds to the chordwise refinement from 100 to 350 points around the airfoil with 220 spanwise points. The lower section corresponds to the variation from 160 to 220 spanwise points with 200 points around the airfoil. Therefore, the 200 × 220 case is repeated in Table 1. The percent change from coarser to finer spacing is reported for each study.

The SA model shows nice convergence characteristics for both thrust and torque based on increased airfoil discretization. Importantly, the thrust and torque values change by less than 0.5% as the chordwise points go from 200 and 350. As expected based on Tran et al., the SA-AFT model is not well converged even with 350 airfoil points. However, a 200-point discretization increase around the airfoil leads to only a 4% prediction difference as opposed to 20% in the airfoil study. For both models, the 350 points case required twice as many core hours as the 200 points case to complete, which is an important consideration given an end goal of simulating complex full quadrotor geometries. To further evaluate the grid refinement, the grid convergence index (GCI) was calculated.

The GCI is a confidence interval introduced by Roache that is used to determine the expected converged solution [44]. Using C_T as a basis for convergence, the GCI of the chordwise refinement for the finest three points, 200–350 points around the airfoil, was found to be 0.06 and 1.23% for the SA and SA-AFT models, respectively. Applying this same calculation to the C_Q, the GCI was again found to be small for the SA model, around 0.01%, and larger for the SA-AFT model, at 2.17%. The finding that torque as predicted using the transition model is most affected by the grid is physically understandable because of the importance of the boundary-layer behavior in the development of torque.

The results of the grid study are also plotted in Fig. 4. The Richardson extrapolation of the finest two points is calculated based on the convergence rate determined using the GCI and included in the

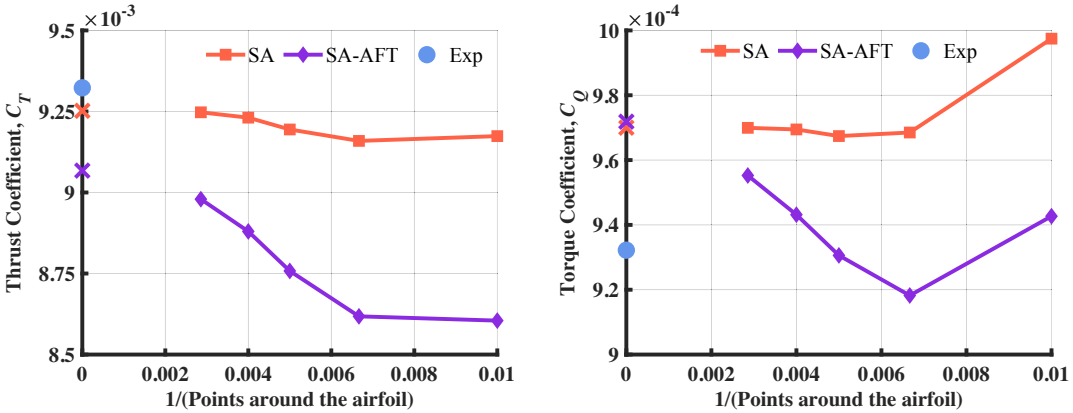

Fig. 4 Grid convergence study of the points around the airfoil for the SA and SA-AFT models. The "×" marks on the *y* axis represent the Richardson extrapolation of the performance values based on the finest three points. The experimental value is plotted here as a blue circle on the *y* axis for reference.

plot as "×" marks on the y axis. Although the SA model is relatively unchanged with increasing resolution, the SA-AFT model is clearly not converged. The converged SA-AFT coefficient of thrust value remains below the SA value while the coefficient of torque value becomes slightly higher. This behavior indicates that the transition model is predicting more separation. It was already demonstrated by Tran et.al. that the transition models come with very heavy grid requirements. This is a tremendous drawback. Here, where the end goal is full simulation of multirotors in flight, it is not feasible to use the indicated grid resolution around the airfoil for convergence of the transition-model-based computation. The very similar converged result for the SA-AFT model and the SA model is noted. The grid resolution of 200 points around the airfoil is used where the SA-AFT gives much lower predictions for the thrust and torque compared with the SA model. The results will be analyzed based on this lower grid resolution.

Another parameter that is related to the boundary-layer resolution is the number of points extending outward from the surface in the near-body mesh. The default in mStrand is 51 points to cover the $0.4\,c$ length region. Table 2 shows that increasing the number of points to 101 does not affect either the SA or the SA-AFT solutions. Although the SA-AFT GCI values are relatively high, it is important to recall that based on Tran et al. this is a high upper bound for the transition models used in this study. Thus it is expected that the other transition models will provide reliable results with 200 airfoil points.

The spanwise grid study used 160–220 points across the blade span in increments of 30. The results, shown in Table 1, yield negligible variations in the C_T and C_Q, with a maximum change at the finest spanwise spacing of 0.12% for both models. While 160 would obviously have been suitable, 220 spanwise points were used in the simulations as shown in Fig. 5.

For the previous runs, the mStrand solver was set to run 5 subiteration steps and the SAMCart solver was set to 10 subiterations, both of which are the default settings in Helios. To test the effect of numerical convergence, a subiteration study was conducted using the SA model. For the chosen grid spacing of 200 points around the airfoil and 220 spanwise points, the number of subiterations was increased to 10 and 20 in mStrand and SAMCart, respectively. In addition, the sensitivity to normal grid spacing was tested by refining from 51 to 101 points in the strand direction while keeping the total strand distance of $0.4c$ constant. The results are shown in Table 2.

For both mesh resolutions, increasing the number of subiterations actually decreases the thrust and torque very slightly. The increase in computational time, however, was twofold. An additional study using the SA-AFT model was conducted with 101 normal points, 10 subiterations in mStrand, and 20 subiterations in SAMCart, representing the finest selection of both parameters. The resultant performance values were $C_T = 8.746\times10^{-3}$ and $C_Q = 9.236\times10^{-4}$, resulting in only a -0.1% change in thrust and -0.7% change in torque from the original settings. Therefore, it was concluded that the subiteration count can be kept at 5 for mStrand and 10 for SAMCart and the wall normal grid resolution was kept to 51 points.

For the full SUI simulations, the fuselage mesh spacing was set to $0.064\ c$ for a total of 1.43×10^5 surface points. This is similar to the surface spacing previously determined to be satisfactory for download prediction [14]. It should be noted that the support structures holding the rotor arms are modeled as airtight in this paper, when in fact they are hollow channels on the real vehicle. This artificial blunt shape may have an effect on the drag due to blockage. However, the effects of this modeling limitation are expected to be small. The fuselage surface mesh is also shown in Fig. 5, with the fuselage volume mesh drawn in red and overlapping the off-body mesh in blue.

Table 2 Results of subiteration study for the SA model

	$C_T, 10^{-3}/C_Q, 10^{-4}$ (CPU hours, 10^4)	
Points (normal)	Coarse subiterations	Fine subiterations
51	9.194/9.674 (4.942)	9.189/9.631 (7.678)
101	9.218/9.691 (7.096)	9.212/9.646 (13.57)
Experiment	9.323/9.322	

2. Off-Body Mesh

The off-body mesh domain for the isolated rotor cases was set to extend 2.54 m in each direction, corresponding to greater than 13.3 times the rotor radius. A fixed refinement region with a spacing of $0.05c$ was set around the rotor $1.25R$ away in each direction in the rotor plane and $0.25R$ above and below the rotor. The off-body mesh shares four overlapping cells with the near-body mesh to allow for flow interpolation. To avoid the transient effects of the starting vortex, adaptive mesh refinement (AMR) was set up to start after the end of the second rotor revolution.

For the full vehicle cases, the off-body mesh was set to 4.064 m in each direction, corresponding to greater than 21.3 times the rotor radius as shown in Fig. 5. To reduce computational costs, a fixed refinement region was not used for the full vehicle cases. Instead, the AMR was set to start earlier, at the end of the first rotor revolution of the slowest rotor.

III. Isolated Rotor Results

To evaluate the predictive capabilities of Helios for small rotorcraft, we first consider the effect of the different turbulence models on the predictions of a single rotor in hover. RPMs ranging from 1500 to 4500 in increments of 1000 RPM are tested. Then, the single rotor in forward flight is simulated at the nominal RPM of 3500 using the fully turbulent model and one of the laminar–turbulent transition models.

A. T-Motor Rotor in Hover

The periodicity of the rotor thrust and torque can be seen in Fig. 6 as well as the effect of the starting vortex. The average force over one rotor revolution is the common metric used to evaluate the performance. Here the average over the 10th revolution is used.

The rotor wakes predicted by the different turbulence models are shown in Fig. 7. A wake is visualized by plotting the isosurfaces of q-criterion ($q = 0.001\ \mathrm{s}^{-2}$) colored by velocity magnitude at the final time step for all RPMs and turbulence models. The fully turbulent SA model lacks the secondary structures that the other models predict. Although the secondary structures were previously thought to be a numerical artifact, they have recently been visualized experimentally by Wolf et al. [45]. Further discussion of the secondary wake structures can be found in Abras et al. [46,47], Hariharan et al. [48], and Bodling and Potsdam [49]. While these flow features have been shown in the above references to have only minimal impact on the integrated forces and moments on the isolated rotor, they may influence the interactional aerodynamics in complex configurations with multiple components. These vortices are captured in the off-body and are resolved by AMR, which means that these flowfields were identified as having much greater vorticity magnitude compared with the strain rate magnitude. Although no comments are made about their source, this flow phenomenon is clearly more prominent in the transition models, especially using SA-AFT, and capturing these flow features is costly due to increased grid size. This is partly responsible for the computational cost difference between the current simulations that will be discussed more thoroughly in the results.

The sectional airloads of the simulations were extracted from the flow solution over the final rotor revolution. The airloads were averaged over the entire rotor revolution to generate a representative spanwise variation of the sectional airloads and plotted along with instantaneous plots of skin friction at the final time step in Figs. 8–11. The forces reported are calculated in the local airfoil frame of the rotor blade section and account for the geometric twist. Thus, they are appropriately named the normal and chordwise force. The SA and SA-AFT models are represented by solid lines, whereas the SA-MB and SA-M15 model lines are dashed.

The transition models predict large amounts of separated flow near the tip, which corresponds to the increased vorticity in the wake depicted in Fig. 7. Although the SA-AFT and SA-M15 models

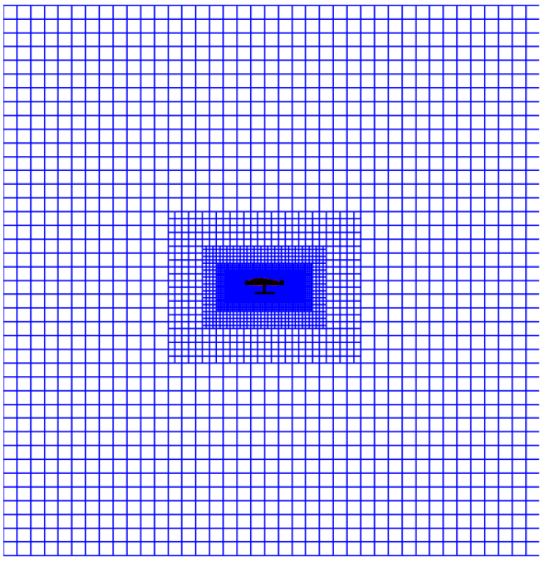

a) The entire computational domain with the off-body mesh in blue and the fuselage surface depicted in the center in black. This image was generated at the start of the simulation, prior to the effects of AMR

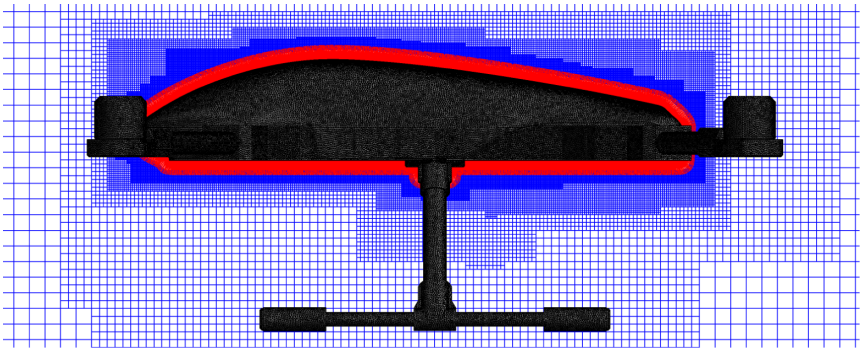

b) Fuselage surface mesh with slice of near-body volume mesh, in red, overlapping the blue off-body volume mesh. The rotors are excluded for clarity

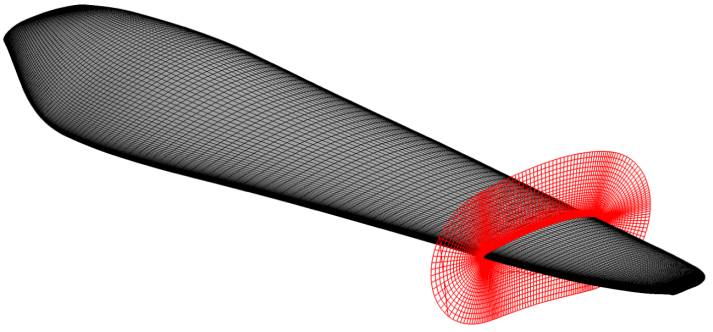

c) Counterclockwise blade surface mesh with a slice, in red, of the near-body volume mesh

Fig. 5 Various views of the representative meshes used in this study.

predict some flow separation near the tip at 1500 RPM, the SA-MB does not. As the RPM increases, the separated regions predicted using the transition models expand further inboard. However, the SA model predicts fully attached flow at all RPMs, leading to higher predicted thrust and torque as shown in Figs. 12 and 13.

Figures 12 and 13 provide the thrust and torque coefficients, averaged over the 10th rotor revolution, from the simulations and experiment. In addition, the comprehensive analysis simulations by Russell and Sekula using a free wake model in CAMRAD II are included as a baseline representation of a lower-fidelity method [50].

Conservative measurement uncertainties were reported for the experiments that accounted for calibration error, hysteresis, repeatability, and unsteady loading [41]. While the uncertainty levels are high (0.6 N for thrust measurements and 0.02 $N \cdot m$ for the torque measurements), the scientists modified their comprehensive analysis multiple times in an attempt to get better agreement with the reported thrust and torque values shown in Figs. 12 and 13. They reported the measurement results for multiple rotors commenting on their differing performance even though for many cases the differences were within the reported uncertainty levels. Therefore, the reported mean experimental value and the trend are used for comparisons made here.

For all of the Helios cases shown, the average thrust and torque values are computed over the ninth and 10th revolution separately. The maximum change in these average thrust and torque values spanned no more than 0.20 and 0.1581%, respectively, across all RPMs and turbulence models considered, demonstrating high temporal convergence. The prediction error discussed in this paper is a relative measure of comparison to the experimental value, rather than a statement of absolute accuracy. A positive percentage difference indicates an overprediction compared with experiments, whereas a

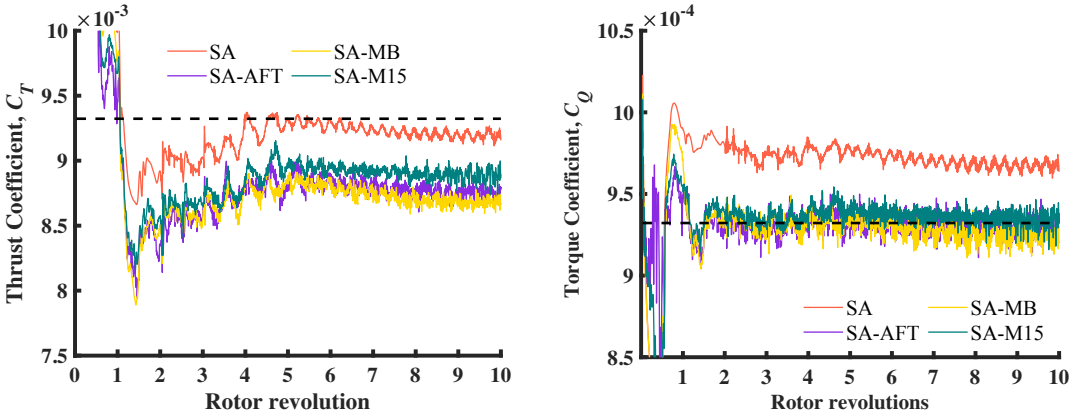

Fig. 6 Simulated torque and thrust coefficients of the isolated T-Motor rotor in hover at 3500 RPM at each time step. Dashed black line represents the experimental value.

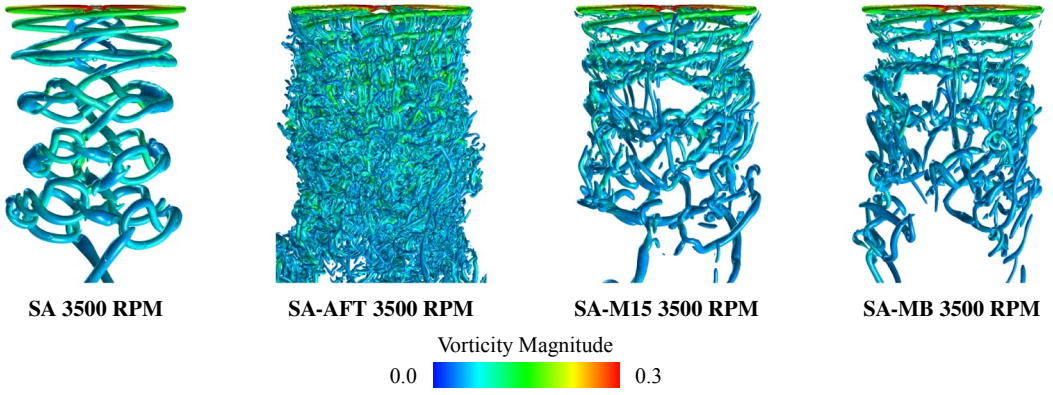

Fig. 7 Isosurfaces of $q = 0.001$ s^{-2} colored by vorticity magnitude at the end of the 10th rotor revolution of the isolated rotor in hover at 3500 RPM with different turbulence models.

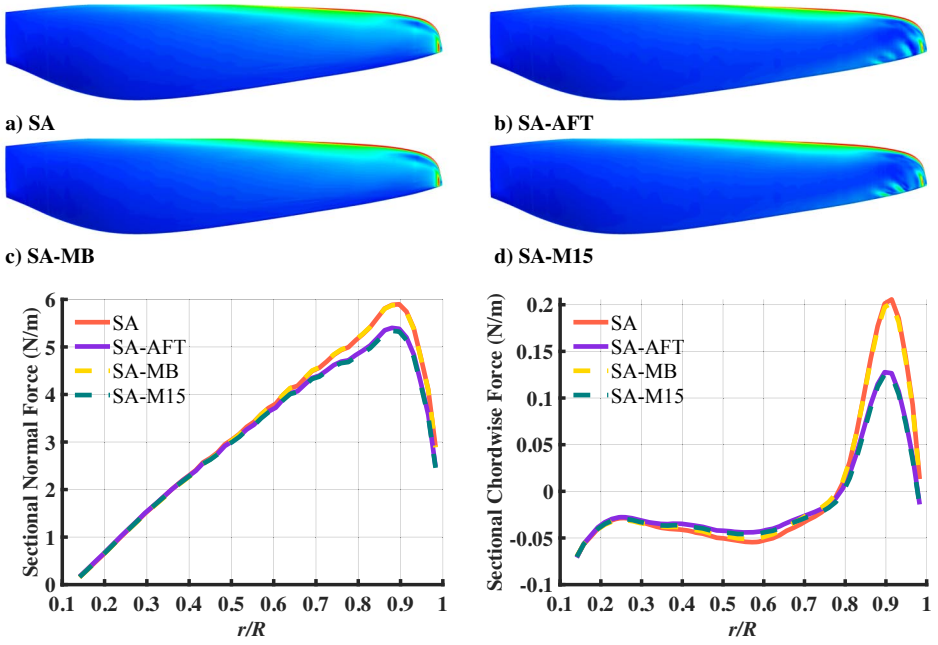

Fig. 8 Instantaneous plots of skin friction at the final time step (a–d) and simulated sectional normal force and chordwise force averaged over one rotor revolution for the isolated T-Motor rotor in hover at 1500 RPM.

negative value indicates underprediction. The prediction error of the comprehensive analysis results is excluded due to its large magnitude: around 10% for thrust and greater than 20% for torque. The very large discrepancy between the comprehensive analysis and the CFD results highlights the benefit of CFD. The SA model provides the thrust prediction closest to the experimental values, with a maximum error around 2.3%. The SA-MB model predicts the highest thrust out of the transition models at 2500 RPM. However, as RPM increases,

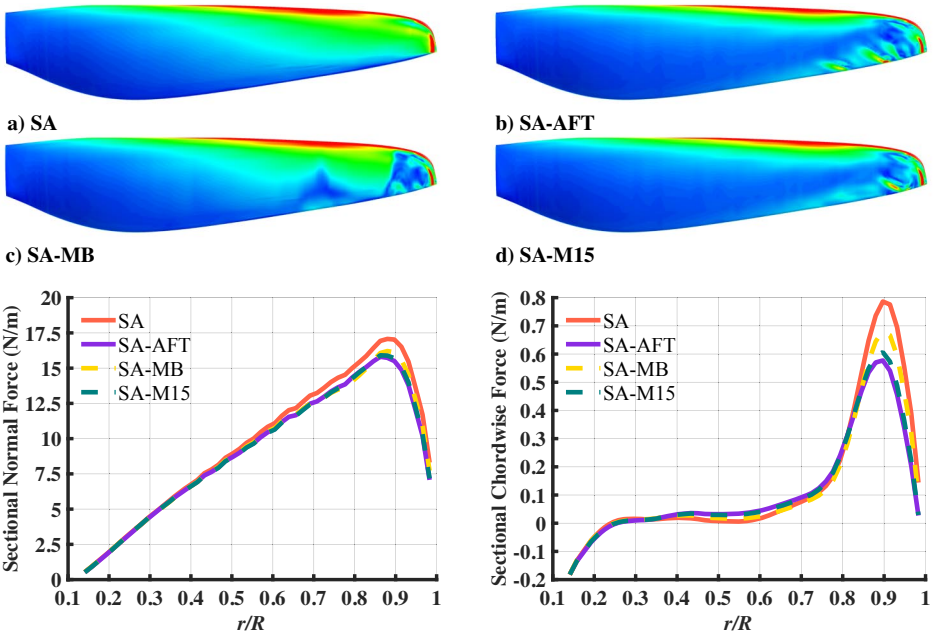

Fig. 9 Instantaneous plots of skin friction at the final time step (a–d) and simulated sectional normal force and chordwise force averaged over one rotor revolution for the isolated T-Motor rotor in hover at 2500 RPM.

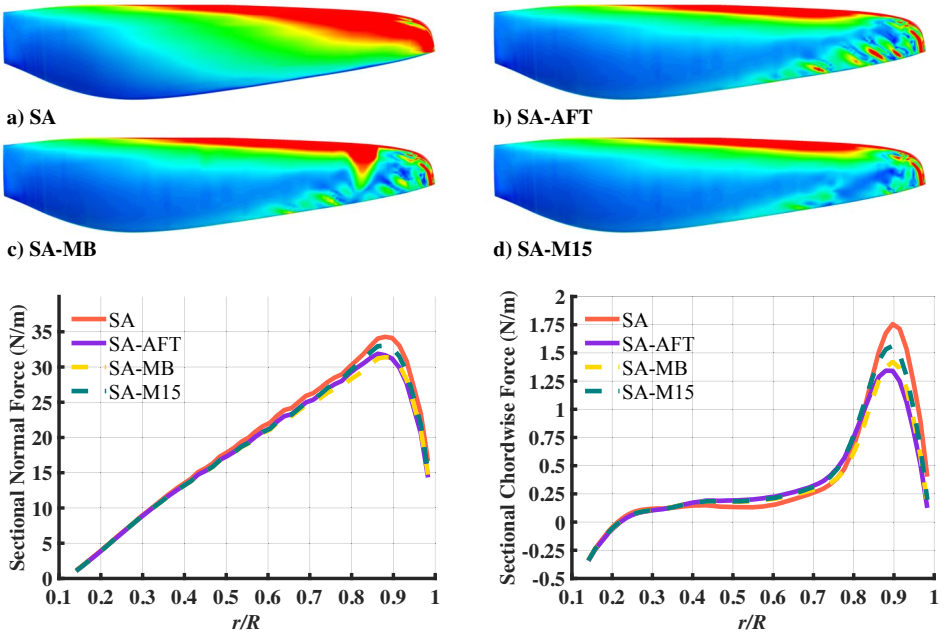

Fig. 10 Instantaneous plots of skin friction at the final time step (a–d) and simulated sectional normal force and chordwise force averaged over one rotor revolution for the isolated T-Motor rotor in hover at 3500 RPM.

the other models show a more steep increase in thrust coefficient, indicating a stronger Reynolds number dependence. The SA-M15 model shows the most significant trend of increasing thrust coefficient with RPM.

All of the CFD simulations underpredict the thrust. It is possible that the inclusion of the rotor hub region would increase the thrust slightly. In addition, slight changes to the rotor geometry change the predictions. CAMRAD II predictions of the T-Motor rotor by Russell et al. overpredicted both thrust and power and required a modification of the twist from the laser scan to match the experimental value [50]. The change in twist was considered because there was doubt concerning the accuracy of the laser scan. A twist decrease of 1 deg was needed for the CAMRAD II analysis to give more accurate results. Preliminary studies using Helios show that a 0.2 deg increase in the twist brings the prediction perfectly in line with the experimental thrust value at 3500 RPM.

The relationship between the torque and RPM is similarly captured quite well across all models. However, the SA model overpredicts the torque, whereas the transition models are close to the experimental data. At the nominal rotor speed of 3500 RPM, the predicted torques of the SA-AFT and SA-M15 models are very close to the experimental value. The SA-MB model demonstrates the strongest torque trend, behaving as a fully turbulent model at the lowest RPM while predicting the lowest C_Q value at the highest RPM. The other models provide good results across all RPMs.

These results can be further evaluated by introducing another important aerodynamic metric for rotorcraft performance, the figure of merit, a measure of hovering efficiency. figure of merit is a

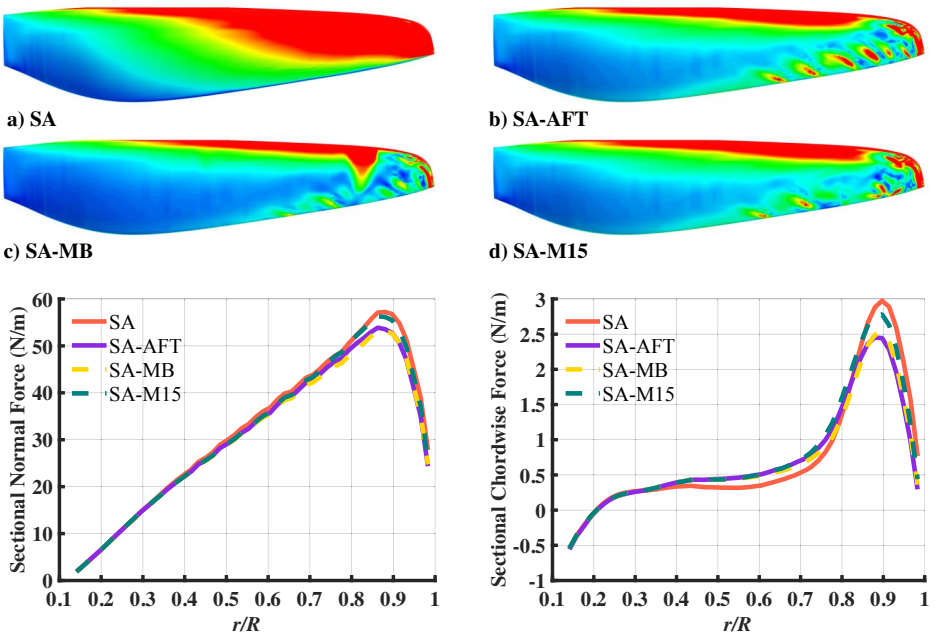

Fig. 11 Instantaneous plots of skin friction at the final time step (a–d) and simulated sectional normal force and chordwise force averaged over one rotor revolution for the isolated T-Motor rotor in hover at 4500 RPM.

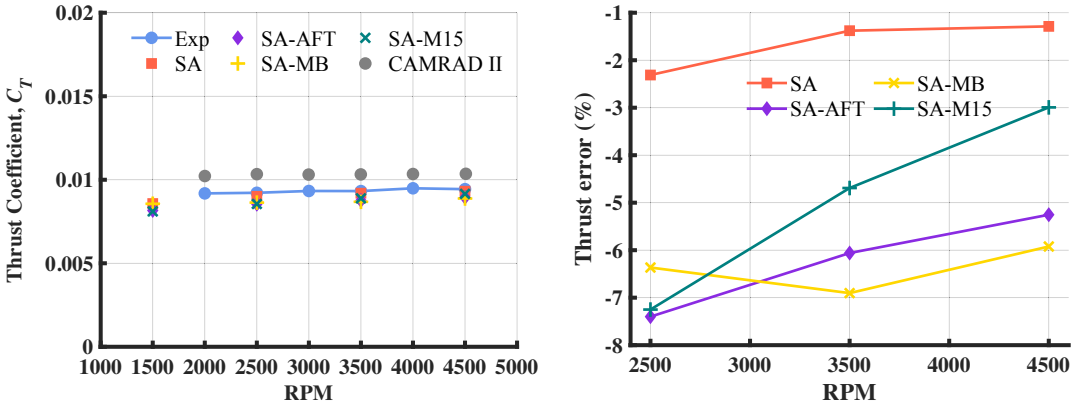

Fig. 12 Thrust coefficient of the isolated T-Motor rotor in hover as a function of RPM. Results are an average of the 10th rotor revolution. CAMRAD II results were digitized from in Russell et al. [50].

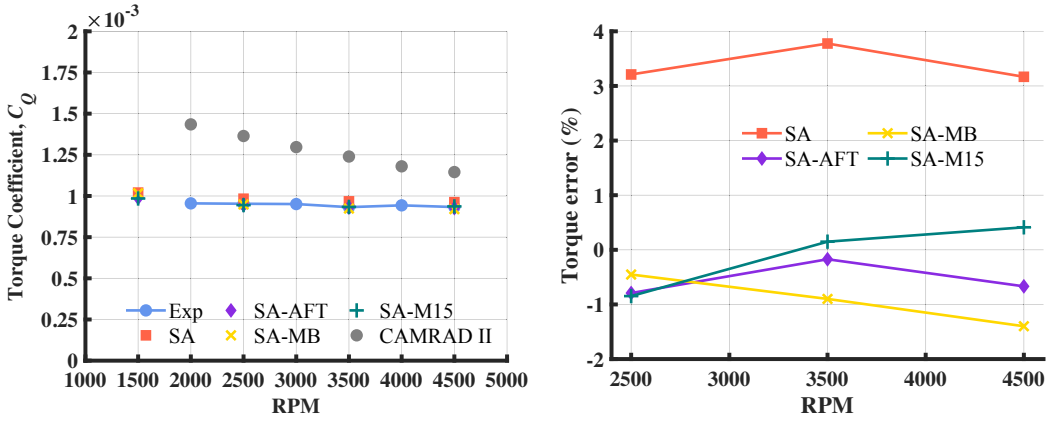

Fig. 13 Torque coefficient of the isolated T-Motor rotor in hover as a function of RPM. Helios results are an average of the 10th rotor revolution. CAMRAD II results were digitized from in Russell et al. [50].

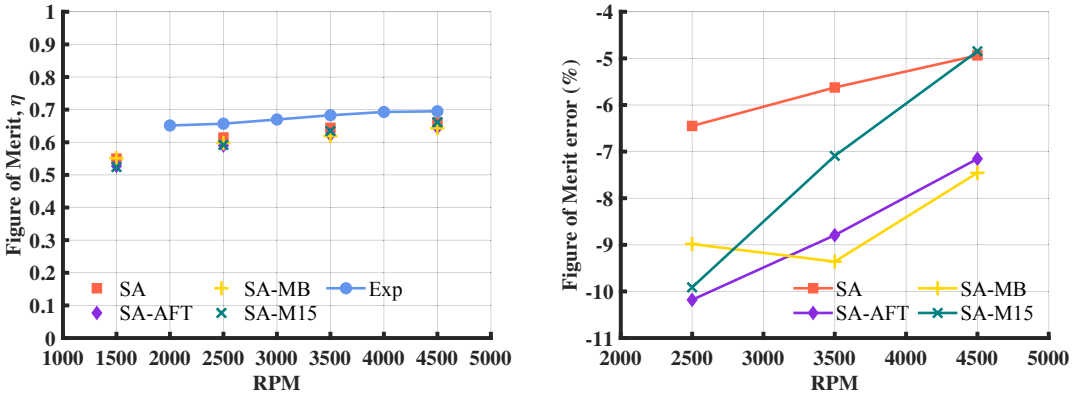

Fig. 14 Figure of merit of the isolated T-Motor rotor in hover as a function of RPM. Results are an average of the 10th rotor revolution.

dimensionless quantity derived from application of momentum theory to a hovering isolated rotor and represents the ratio of ideal to actual power, therefore yielding a possible range from 0 to 1 [51]. Figure of merit is calculated as a function of thrust, torque, rotor area, fluid density, and rotor speed:

$$FM = \frac{\text{Ideal power}}{\text{Actual power}} = \frac{\sqrt{T^3/2\rho A}}{Q\Omega} = \frac{C_T^{3/2}/\sqrt{2}}{C_Q} \tag{2}$$

The figure of merit is plotted and compared with the experimental values in Fig. 14. Clearly, thrust has a larger influence than torque in the figure of merit equation. Therefore, the prediction of figure of merit is much better with the SA model. However, the improvement in thrust with increasing RPM by the SA-M15 model, combined with accurate torque prediction, yields the closest figure of merit prediction at 4500 RPM across all models. Further study of the surface flow characteristics, such as coefficient of pressure and skin friction, are shown in the Appendix.

All predictions, with or without a transition model, landed within the experimental uncertainty. Unfortunately, there are no rotor surface measurements from experiments to better detail the flowfield for these rotors. In addition, there are concerns about the geometry specification based on the laser scan that can lead to variations in the performance. Therefore, although we are able to comment on the differences in the transition model, we are not able to justify choosing one based on prediction accuracy alone. The computational cost of the isolated rotor in hover cases is shown in Fig. 15. There is a sharp increase in cost for the SA model case at 3500 RPM. This specific case was run on a different computing cluster, and therefore the computational performance cannot be directly compared. The increase in time for the transition models is caused by both the calculation of the extra transition equations as well as the increase in number of cells in the off-body due to AMR. The SA-AFT model, which predicted the most secondary vortices, yielded the highest computational cost. The SA-M15 model was the most efficient transition model throughout these simulations, with slightly faster computational time than the SA-MB model. Therefore, based on the available experimental data and computational cost, the SA-M15 model was chosen as the representative transition model for the forward flight studies.

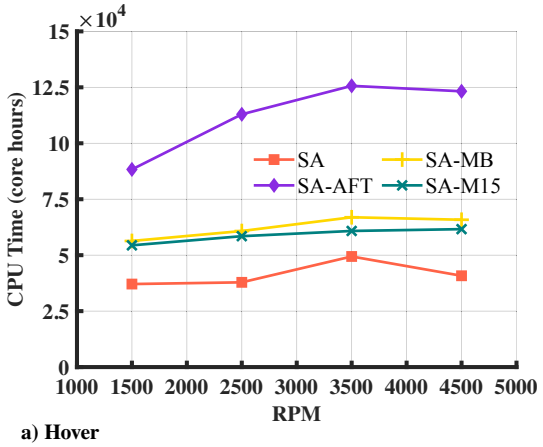

a) Hover

Fig. 15 Computational cost of the isolated rotor hover cases.

B. T-Motor Rotor in Forward Flight

The flight conditions of the forward flight cases were selected from the same study of multirotors conducted at NASA Ames [41]. The relative wind speed was about 20 ft/s with rotor pitch angles varying between 0.11 and −19.92 deg, with negative numbers discerning a pitch-down angle. The rotor speed chosen was 3500 RPM. It should be noted that, although the speed of the forward flight cases is labeled 20 ft/s, the measured wind speed during the forward flight tests at 3500 RPM varied between 19.42 and 19.91 ft/s. The simulations performed for this study account for these slight discrepancies, which are included in the technical report [41].

The coordinate system reported in this paper was chosen to match that in the technical report with positive rolling moment M_x to the right, positive pitching moment M_y nose up, and positive yawing moment M_z nose right [40,41]. Similarly, the reported thrust is defined in the plane of the rotor to align with the load cell. The rotor thrust F_z points positive upward from the rotor plane.

The rotor thrust coefficient over the entire simulation is plotted in Fig. 16. As expected, the forward flight simulations converge much faster than the hover cases because the relative wind is able to quickly push the effects of the starting vortex away from the rotor. It is noted that the average thrust changes at most by 0.0813% between the ninth and 10th rotor revolutions across all pitch angles. The flow is represented visually in Fig. 17, where the isosurfaces of q-criterion equal to 0.001 are plotted for the final time step (end of eighth rotor revolution) for the isolated rotor cases at 0.11 and −19.92 deg pitch angles. Secondary structures occur at all pitch angles in forward flight, although they are more pronounced at higher pitch angles.

The instantaneous skin friction at various azimuthal angles over the final rotor revolution is plotted for the 0.11 deg pitch and −19.92 deg pitch cases in Figs. 18 and 19. The 90 deg azimuth and 270 deg azimuth represent the advancing and retreating sides of the blade, respectively. The polar contour plots representing the sectional normal force around the rotor azimuth for the final rotor revolution are shown in Fig. 20. Shown are the results for the SA and SA-M15 models for the 0.11 and −19.92 pitch angles, as well as the difference between them. A positive value in the difference plots indicates higher predicted force by the SA model. The simulated rotor rotates counterclockwise in the direction of positive azimuth angle.

Both the SA and SA-M15 models demonstrate some separation past $r/R = 0.5$ at the 180 deg azimuth location and near the tip at the 270 deg azimuth location at 0.11 deg pitch. Therefore, at the 180 and 270 deg locations, there is minimal difference in sectional normal force for the 0.11 deg pitch case, as shown in Fig. 20. However, although the SA model predicts attached turbulent flow at the 0 and

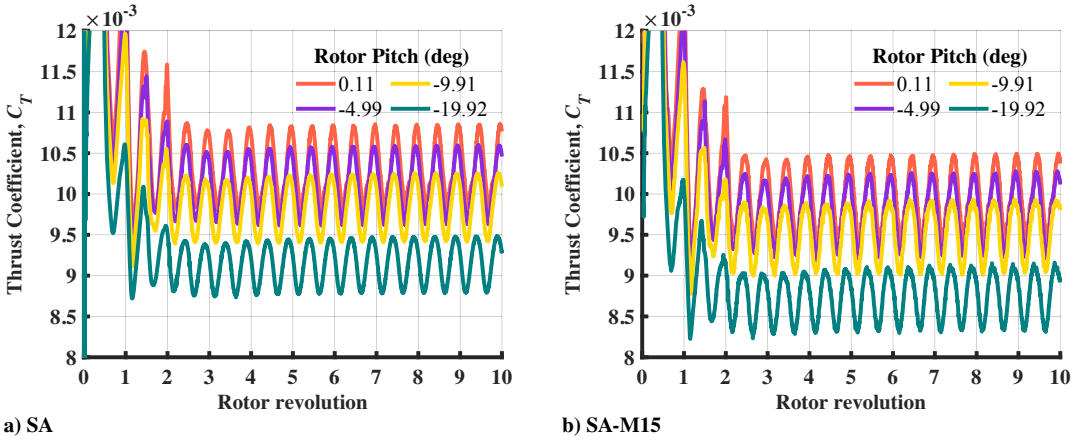

a) SA b) SA-M15

Fig. 16 Simulated thrust of the isolated T-Motor rotor in 20 ft/s forward flight at 3500 RPM over all time steps.

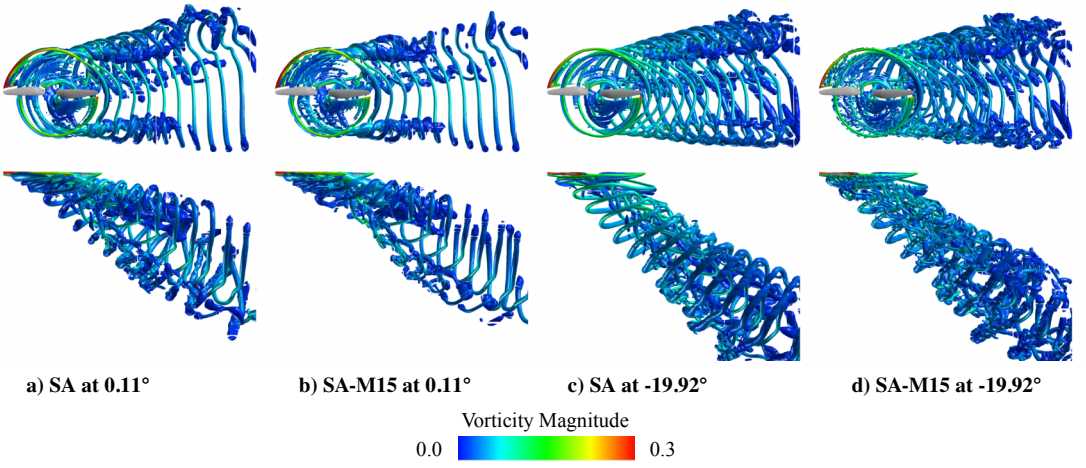

a) SA at 0.11° b) SA-M15 at 0.11° c) SA at -19.92° d) SA-M15 at -19.92°

Fig. 17 Isosurfaces of $q = 0.001$ s^{-2} at the end of the 10th rotor revolution of the simulated isolated T-Motor rotor in forward flight. Images were taken in the rotor plane.

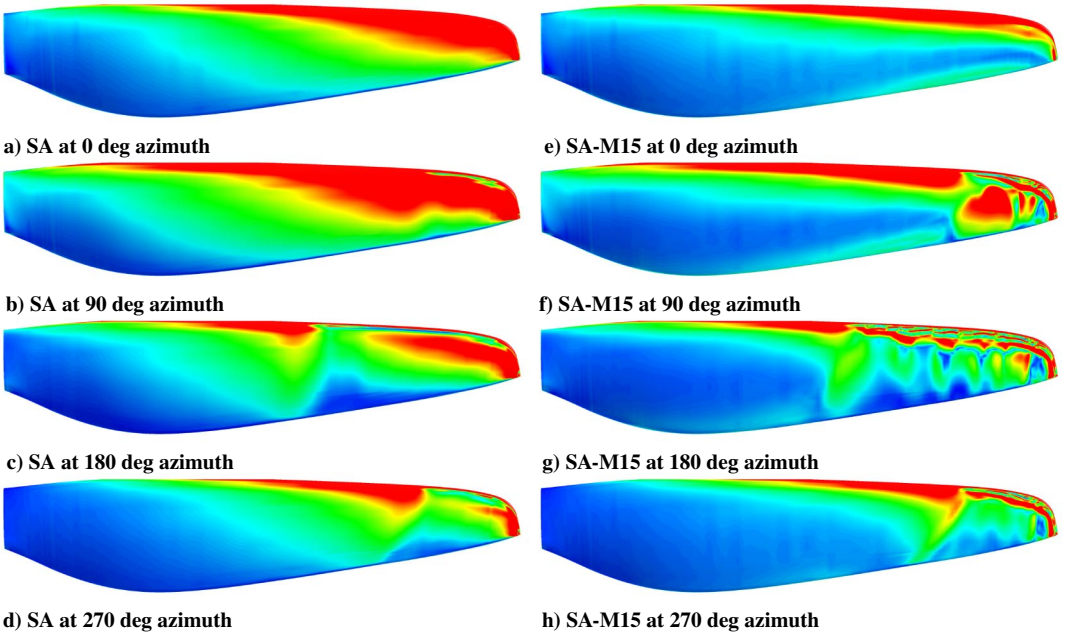

a) SA at 0 deg azimuth
e) SA-M15 at 0 deg azimuth
b) SA at 90 deg azimuth
f) SA-M15 at 90 deg azimuth
c) SA at 180 deg azimuth
g) SA-M15 at 180 deg azimuth
d) SA at 270 deg azimuth
h) SA-M15 at 270 deg azimuth

Fig. 18 Instantaneous plots of skin friction over the final rotor revolution for the T-Motor rotor in forward flight at 0.11 deg pitch.

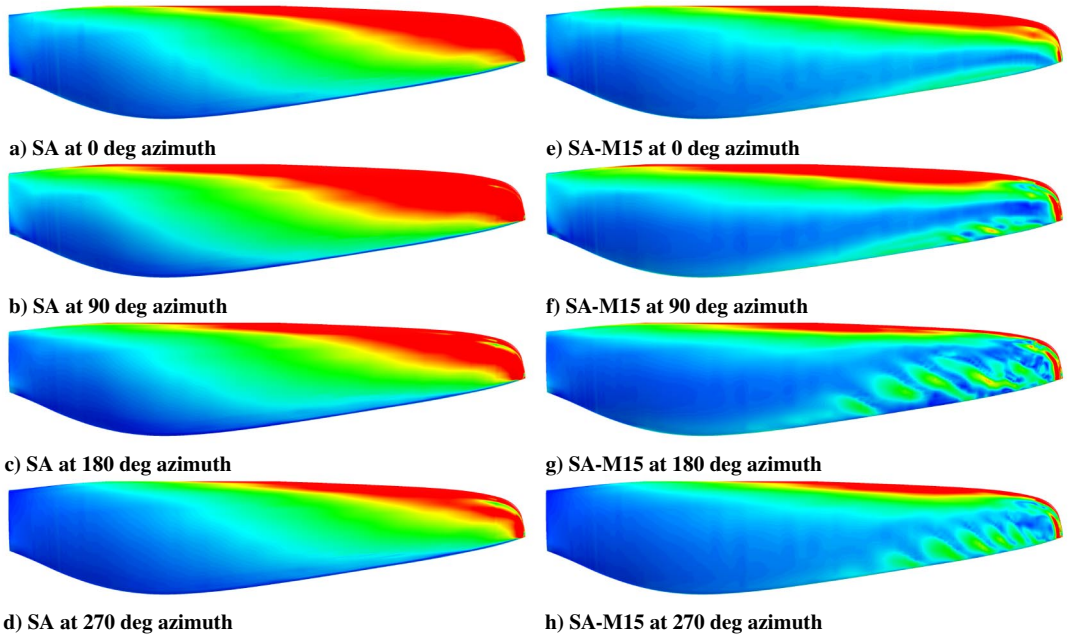

Fig. 19 Instantaneous plots of skin friction over the final rotor revolution for the T-Motor rotor in forward flight at −19.92 deg pitch.

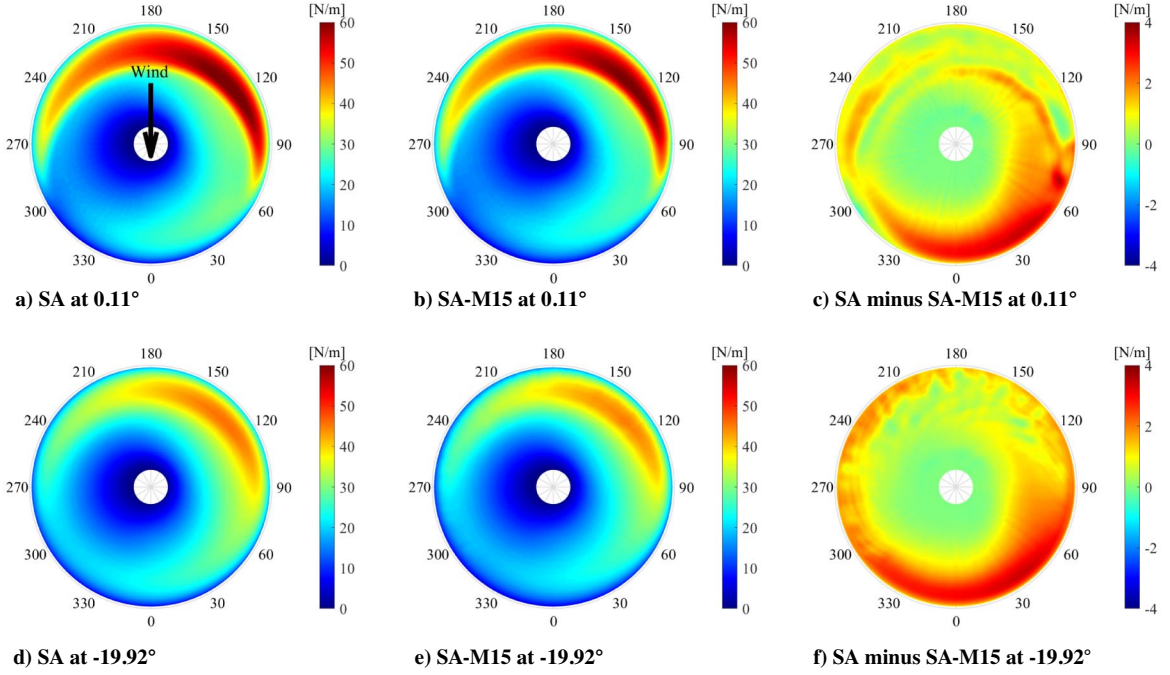

Fig. 20 Normal forces on isolated rotor in forward flight for the SA model, the SA-M15 model, and the difference between the results of each. The wind direction is labeled in (a).

90 deg azimuth locations, the SA-M15 model predicts transitional flow at 0 deg azimuth and separated flow at the 90 deg azimuth location. The greatest difference between the models occurs in this portion of the rotor rotation between 0 and 90 deg, likely due to the change in induced velocity and angle of attack during the transition from the retreating to advancing side of the blade.

For the −19.92 deg pitch case, the flow stays fairly attached using the SA model. However, the flow is mostly separated near the tip using the SA-M15 model. The exception to this observation occurs when the blade is passing from the retreating to advancing side and appears to stay attached, which may be due to a spanwise flow effect. The transition from retreating to advancing side matches the findings from the 0.11 deg condition. The change in relative velocity due to the forward flight condition introduced interesting flow effects that were not seen in hover. For example, the 0.11 deg pitch angle is able to induce flow separation for the SA model due to the change in relative velocity and angle of attack.

The predicted forces and moments of the T-Motor rotor in 20 ft/s forward flight at multiple pitch angles are plotted in their dimensional form against experimental data in Fig. 21. There were several key modeling limitations that impact the results of the simulations and distinguish the computational representation from the physical setup of the experiments. For example, neither the rotor hub nor the load cell assembly was modeled in the simulations. In addition, the wind tunnel walls were excluded from the computational domain. The rotor drag force F_x and side force F_y predictions are not discussed as the peak measured loads were much lower than the reported uncertainties of 0.396 and 0.250 N, respectively.

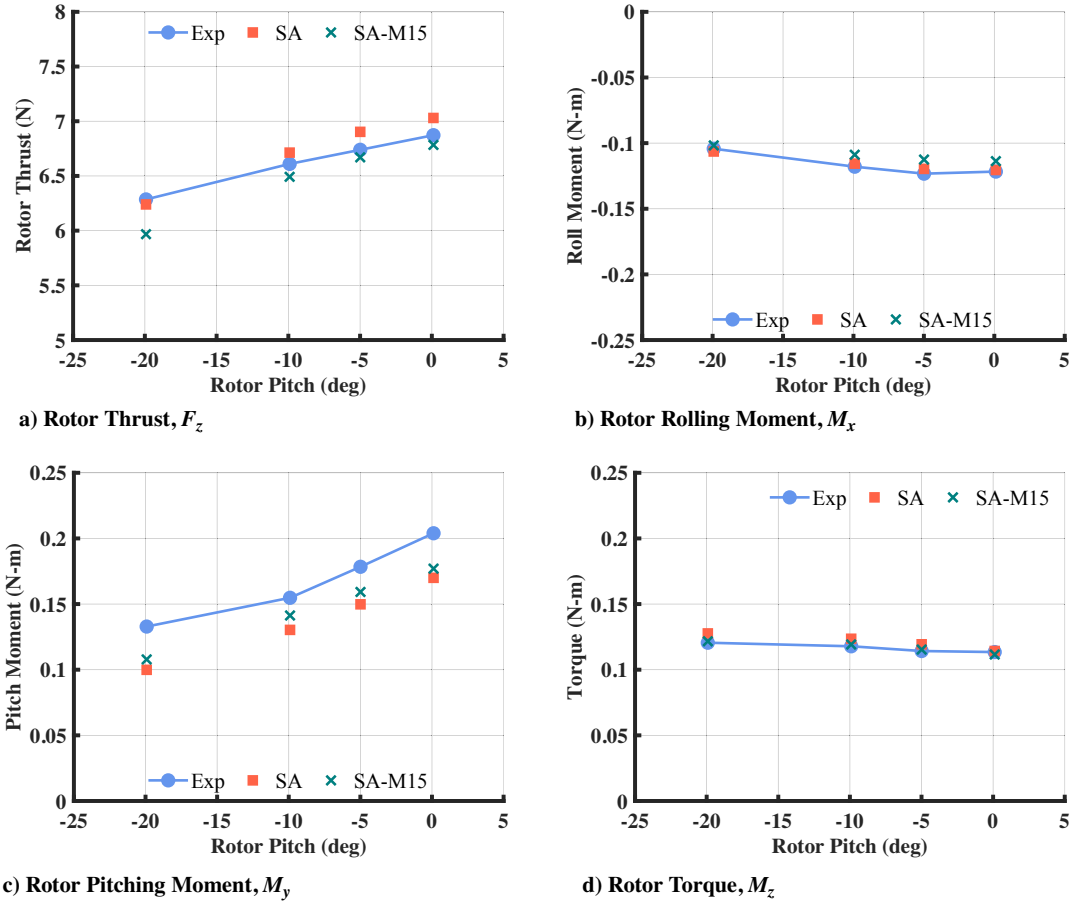

Fig. 21 Predicted thrust, rolling moment, pitching moment, and torque on the isolated T-Motor rotor in 20 ft/s forward flight at 3500 RPM. Results are an average of the 10th rotor revolution.

As the rotor pitches negatively, the relative wind decreases the angle of attack on the advancing side, which has the higher local flow speed reducing the overall thrust. Therefore, of the pitch values measured, the rotor thrust should be highest at 0.11 deg as is the case in Fig. 21. Both models show a similar trend with pitch angle and demonstrate less than 5% deviation from the experimental thrust values. The separated flow predicted by the SA-M15 model again leads to lower thrust compared with the SA model.

The rolling moment is expected to be negative due to the higher normal force on the advancing side, causing a leftward roll. The SA model predicts greater normal forces than the SA-M15 model on the advancing side, which enhances the difference between the advancing and retreating side, resulting in a greater magnitude rolling moment. The rolling moment error is less than 3% for the SA model and 9% for the SA-M15 model for the flight conditions simulated. The cause of the difference is highlighted in Figs. 20c and 20f, where the predicted normal forces differ most near the tip of the rotor blade as the rotor enters the advancing side of the azimuth.

The pitching moment is positive, indicating a pitch up, due to the high normal force at the front of the rotor disk. Because SA predicts higher normal force in the rear of the rotor disk, as shown in Figs. 20c and 20f, the resultant pitching moment is lower than the SA-M15 model. The pitching moment magnitude is predicted poorly, with up to 25% error with the SA model and 19% error using the SA-M15 model. However, the exclusion of the rotor hub region, which represents over 12% of the rotor radius, may account for the underprediction of the pitching moment.

As the pitch-down angle increases, the reduction in the relative angle of attack for the blade causes the drag to increase. Therefore, the torque, or yawing moment, should decrease from −19.92 to 0.11 deg. Although both models overpredict the torque, the experimental trend is captured well overall. As expected, the SA model predicts greater torque than the SA-M15 model, reflecting the skin friction plots shown in Figs. 18 and 19. The torque error for both models reflects that of the hover case, with less than 6% error for the SA model and less than 2% error for the SA-M15 model.

After reviewing the prediction of the forces and moments, it is still unclear whether the implementation of the fully turbulent or the transition model yields better accuracy. The total computational cost in CPU hours of the isolated rotor cases for the forward flight conditions is plotted in Fig. 22. For the hover cases, the SA-M15 model increased near-body solution time by approximately 3.5 s per time step, whereas the off-body solution and adaptation time cost an extra 6 s per time step. In forward flight, the SA-M15 model increased

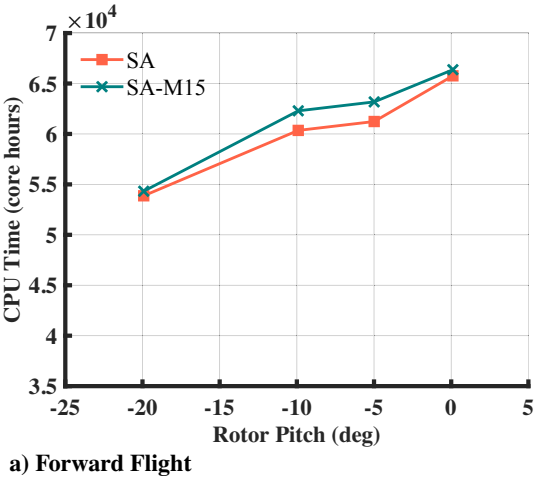

Fig. 22 Computational cost of the isolated rotor forward flight cases for the SA and SA-M15 models.

the near-body solution time of the forward flight cases by 0.9 s per time step, whereas the increase in off-body solution and adaptation time was only 0.5 s per time step. There is a larger cost of implementing the transition model in hover due to the prediction of secondary vortices, shown in Fig. 7, that increases the total number of cells in the off-body due to AMR. Nonetheless, the SA-M15 model is still more expensive in every flight condition. The SA-M15 model does not seem to significantly improve results compared with experiments, yet it increases the computational cost.

IV. Full Quadrotor Results

Full quadrotor simulations were performed in order to ascertain how Helios with near-body solver mStrand performs for a small multirotor.

A. SUI Endurance in Hover

The fully turbulent SA model was selected for the simulation of the SUI Endurance quadrotor. To ensure overlap with experimental data, the quadrotor was simulated with rotor speeds ranging from 1500 to 4500 RPM in increments of 1000 RPM. The rotor plane forces and overall vehicle moments are balanced in the hover configuration due to the counter-rotating rotors that are placed symmetrically about the vehicle. As a result, total thrust, which encapsulates the rotor thrust, fuselage download, and any other interactional effects, is the only significant aerodynamic force. In this paper, thrust coefficient for a quadrotor is calculated differently from that of the isolated rotor to account for the multiple rotors. To ensure that the C_T values are comparable, the quadrotor thrust is divided by the number of rotors. This thrust coefficient is used as a temporal convergence metric and plotted over all time steps for each simulated RPM in Fig. 23.

In hopes of decreasing the number of revolutions required for the full quadrotor simulations, the average thrust and torque from revolution to revolution for the isolated rotor cases were analyzed. The isolated T-Motor rotor in hover converges with a threshold of 1% by the sixth revolution. To ensure convergence, the full quadrotor in hover was simulated for a total of eight revolutions. For the forward flight cases, the maximum change in average thrust dips below the 1% threshold between the third and fourth revolutions across all flight conditions. The torque shows a similar relationship, with a maximum change of 0.81% between the third and fourth revolutions. Therefore, the full quadrotor in forward flight was simulated for a total of six revolutions. Because of the differing rotor speeds in forward flight, the slowest rotor is used as a time-step reference to ensure that all rotors experience at least six revolutions.

The thrust coefficient for the SUI in hover based on the mean of the eighth rotor revolution is plotted in Fig. 24. The thrust coefficient is within 1.7% of the experimental data across all RPMs, which is reasonable given the single rotor outcomes. Again, the underprediction of the thrust may well be due to the rotor geometry specifications. The

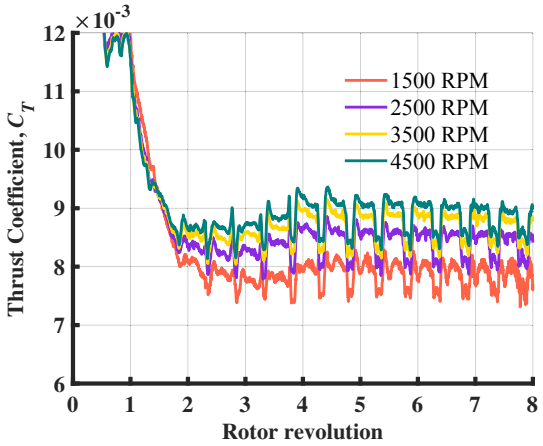

Fig. 23 Simulated thrust coefficient of the SUI Endurance in hover using the SA turbulence model over all RPMs over all time steps.

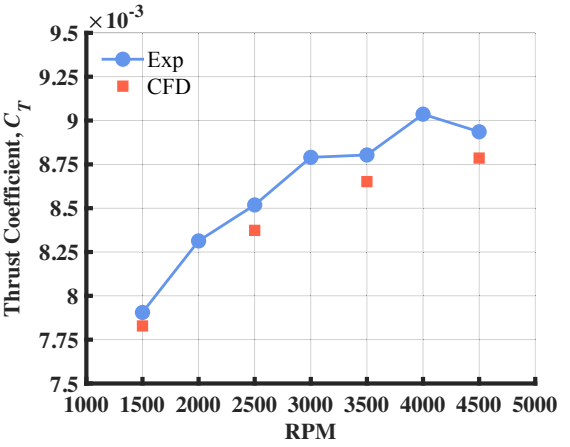

Fig. 24 Simulated thrust coefficient of the SUI Endurance in hover. Results are an average of the eighth rotor revolution.

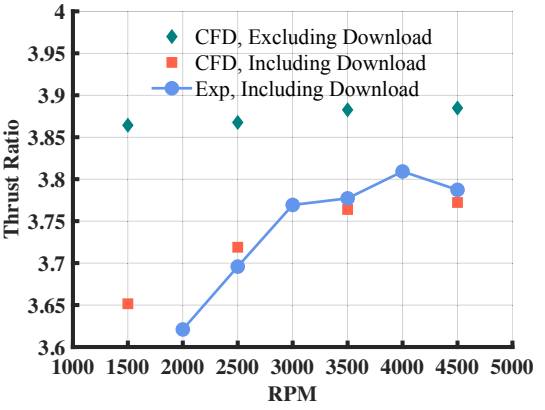

Fig. 25 Thrust of the SUI Endurance in hover normalized by the thrust of the isolated T-Motor rotor.

similar agreement for the full quadrotor and the single rotor indicates well-resolved interactions between the rotors and the fuselage, which consist of both fuselage download and rotor–rotor interactions.

To highlight the relative influences of the hover interactions, the ratio of the total thrust of the full quadrotor to the thrust predicted in the isolated rotor simulations is plotted in Fig. 25. As expected, the fuselage download reduces the overall thrust, leading to a maximum ratio of about 3.8. Even when the negative thrust from the downloaded is excluded, the thrust ratio is still less than 3.9, which highlights the influence of the rotor–rotor interactions. A computational study by Yoon et al. showed that increasing separation distance between the rotors reduces the rotor–rotor interaction and increases the overall thrust [23].

B. SUI Endurance in Forward Flight

The SUI Endurance was simulated in forward flight at 20 ft/s with the fore rotors rotating at 3200 RPM and the aft rotors rotating at 3800 RPM. This flight condition was chosen because it is the closest representation of a realistic flight scenario. To counter the pitching moment induced by the drag on the vehicle, the RPM of the aft rotors must be greater than that of the fore rotors. In addition, the vehicle must have a negative, or nose-down, pitch angle, to generate a forward thrust. Therefore, this configuration was simulated at −4.98 and −9.90 deg, which correspond to the experiments by Russell et al. [41].

It has become more popular to use detached eddy simulation (DES) for rotorcraft simulations [5,14,18,24,26]. Detached DES is a hybrid model that enables RANS when the turbulent scales need to be modeled (i.e., very close to solid surfaces) and turns on large-eddy simulation when the grid scales can resolve turbulent structures. Jia and Lee [52] explored the effect of DES on aerodynamic performance prediction for a coaxial rotor and found that turbulence

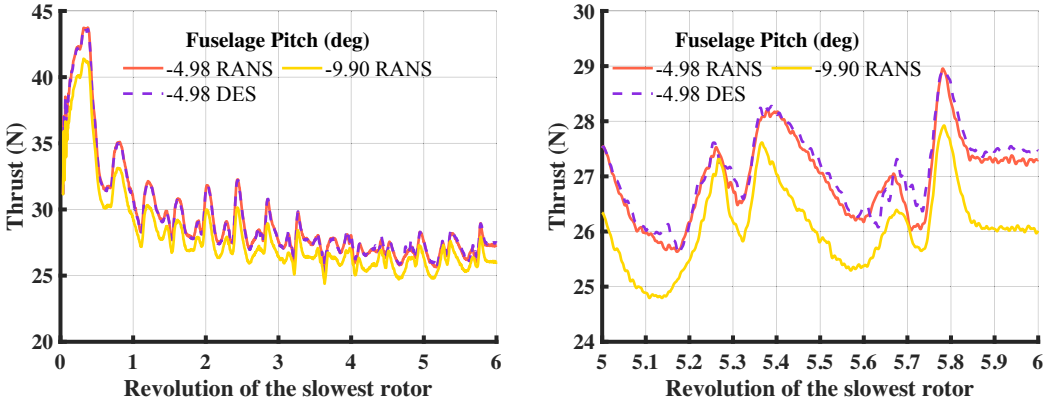

a) Entire simulation b) Final revolution of slowest rotor

Fig. 26 Simulated thrust of the SUI Endurance in 20 ft/s forward flight over time.

modeling selection had minimal effect on airloads and acoustics. The effect of DES on simulation of a multirotor is of particular interest because of the increased interactions. DES is computationally expensive. As such, it was only enabled for the −4.98 deg case because smaller pitch down angles tend to have more pronounced interactions. The experiments also showed higher measured overall drag and thrust at the −4.98 deg condition.

Because of the differing fore and aft rotor speeds, the dimensional thrust, rather than a thrust coefficient, is plotted in Fig. 26. The thrust is shown to stabilize after five rotor revolutions for all cases, and the thrust average does not change by more than 0.6% between the fifth and sixth revolution of the slowest rotor for any simulation. The final revolution of the slowest rotor is plotted in Fig. 26b to show the difference between the RANS and DES results, which is small.

In forward flight, the significant forces and moments are expected to be the thrust, drag, and pitching moment. The side force, yaw moment, and roll moment are negligible due to the symmetry caused by the counter-rotating rotors. For comparison with the experimental work of Russell et al., the moments were measured in the rotor plane, equidistant from the four rotors [41]. Also, the forces and moments are again calculated in the reference frame of the load cell, which means that the drag is simply F_x, irrespective of the pitch angle. The results are tabulated in Table 3. The change in the aerodynamic quantities between the two pitch angles is calculated and shown in the Δ column. The relative error is shown in parentheses.

The computations do a good job of capturing the thrust magnitude in forward flight at both pitch angles. They also do an excellent job of computing the relative difference in thrust between the two pitch angles, with difference from experiments of only 0.37%. Therefore, it seems that the change in thrust is captured very well.

The drag predictions, on the other hand, did not compare well with experiments. The drag error was as high as 13.6%, and the relative difference in drag between the pitch angles was not captured well. Although the CFD did measure a reduction in drag with an increase in the pitch-down angle, the relative difference was 31.7% different compared with that measured in the experiment. The overprediction of the drag is possibly because the fuselage's support structures were modeled as airtight, rather than hollow.

The difference between the RANS and DES is largest for the pitching moment, which is extremely sensitive to the center of gravity (CG) location. Although the computations were set up to match the experimental CG, a deviation of less than 0.01 m in the x direction is able to zero the pitching moment in all simulations. Therefore, the trend with pitch down angle is discussed as opposed to the actual

Table 3 Thrust, drag, and pitching moment of the SUI Endurance in 20 ft/s forward flight

	−4.98 deg			−9.90 deg		Δ	
Quantity	Exp.	SA-RANS	SA-DES	Exp.	SA-RANS	Exp.	SA-RANS
Thrust (N)	27.56	26.97 (−2.1)	27.10 (−1.7)	26.65	26.06 (−2.2)	0.911	0.909 (0.37)
Drag (N)	2.38	2.66 (11.8)	2.65 (11.5)	2.28	2.59 (13.6)	0.093	0.064 (31.7)
Pitching moment (N · m)	0.031	−0.032	−0.058	−0.158	−0.230	0.190	0.197 (3.86)

Error percentages are in parentheses. The Δ column represents the difference between the results at the −4.98 deg and −9.90 deg pitch angles.

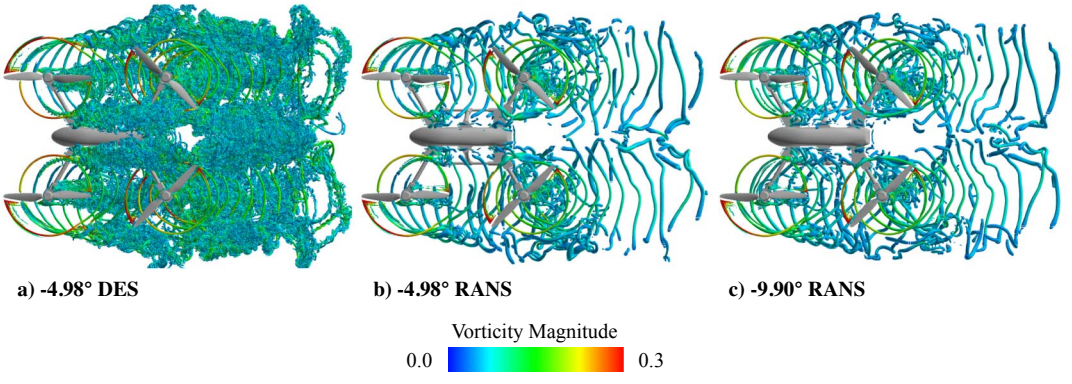

a) -4.98° DES b) -4.98° RANS c) -9.90° RANS

Fig. 27 Isosurfaces of $q = 0.001$ s^{-2} at the end of the sixth rotor revolution of the simulated SUI Endurance in forward flight.

values. The relative difference between the pitching moment for the −4.98 and −9.90 deg cases was captured extremely well by the CFD. The change in pitching moment between flight conditions was predicted within 3.86% error.

Finally, the isosurfaces of q-criterion equal to 0.001 for the SUI Endurance in forward flight are plotted in Fig. 27 for reference. The DES method predicts many secondary structures in the wake that the RANS using the SA model does not, indicating again higher vorticity magnitude compared with strain rate identified by the AMR algorithm. The wake structures seem to originate from an instability in the wake after one half revolution, which is different from the secondary structures seen in the isolated rotor cases when transition models were used. In that case the structures appeared at the wake formation point. Even though for the quadrotor case there is interaction between the wakes and the fuselage and downstream rotors, the wake vorticity has negligible impact on the integrated aerodynamic quantities. This result implies that the DES model is not necessary for prediction of aerodynamic performance especially considering the increase in computational cost. For comparison, both of the −4.98 deg cases were run on 1584 cores, but because the generation of secondary structures predicted by the DES model triggered more AMR, the DES simulation was more costly. The RANS case only required 11 days of wall-clock time, whereas the DES case required 15 days.

V. Conclusions

In this study, the rotorcraft simulation suite HPCMP CREATE-AV Helios with mStrand selected as a near-body solver was assessed for prediction of the aerodynamics of the SUI Endurance quadrotor. The hypothesis that a laminar–turbulent transition model should be used because of the lower-Reynolds-number operating condition of such small rotorcraft was investigated. The following conclusions were drawn from this study:

1) The SA-AFT transition model is more sensitive to rotor blade surface grid resolution than the standard fully turbulent SA model. The SA model demonstrates reasonable performance predictions for all surface grid resolutions tested.

2) In hover, the transition models predicted flow separation that led to vortex shedding and lower thrust and torque compared with the fully turbulent model.

3) The SA-M15 model predicted a stronger trend with RPM (i.e., Reynolds number) than indicated by the experimental data.

4) The SA and SA-M15 models demonstrated the lowest computational cost in this study and predicted the closest figure of merit compared with the experimental data and therefore were selected for the forward flight studies of the single rotor.

5) In forward flight, both the SA and SA-M15 models provided reasonable performance predictions that lie within the experimental uncertainty. The computational cost of implementing the SA-M15 model was higher.

6) The simulations of the full SUI Endurance quadrotor in hover and forward flight using the SA model showed good agreement with experimental data. The thrust was predicted well in all flight conditions, and the drag in forward flight was reasonable provided the limitations of the computational model. Although the CFD failed to capture the pitching moment magnitude, its trend with pitch-down angle was resolved well.

7) An additional DES calculation gave similar results to the unsteady RANS solver, implying that the secondary structures in the wake are not important for aerodynamic performance even when there is interaction between wakes and rotors.

Overall, the fully turbulent SA model provided accurate aerodynamic performance predictions with reasonable computational cost. The transition models did not result in a definitive improvement over the fully turbulent results but did incur increased computational cost. The computations are dependent on an imperfect geometry specification due to difficulties in creating an accurate laser scan of the SUI rotor, which is quite thin. The experimental uncertainty was relatively high. Improvements in either of these would enable more precise assessment of the predictions. Even more helpful would be experiments that better characterize the surface aerodynamics, such as pressure or skin friction. For now, it is recommended that small rotorcraft performance simulations with Helios using mStrand can use the fully turbulent SA model.

Appendix: Further Investigation of the Isolated Rotor in Hover

To further investigate the isolated rotor performance in hover, the pressure and skin friction were extracted from cross sections of the blade corresponding to spanwise coordinates ranging from $r/R = 0.2$ to $r/R = 0.9$. The surface flow variables were extracted from the solution at every other time step and averaged over the final rotor revolution. Therefore, they are not reflective of the vortex shedding behavior predicted by the transition models. The dynamic pressure used to nondimensionalize the aerodynamic coefficients was determined based on the theoretical relative velocity at each cross section of the blade in order to relate the varying rotor speeds. Therefore, the coefficient of pressure is determined as

$$C_p = \frac{p - p_\infty}{(1/2)\rho_\infty((r/R)\Omega)^2} \tag{A1}$$

Similarly, the coefficient of skin friction is

$$C_f = \frac{\tau}{(1/2)\rho_\infty((r/R)\Omega)^2} \tag{A2}$$

The coefficient-of-pressure results for the 2500 and 4500 RPM cases are shown in Fig. A1. The SA and SA-AFT models are again shown as solid lanes, and the SA-MB and SA-M15 models are dashed lines. The rotor section shape is shown, in black, at the bottom of each pressure plot. The Reynolds number, calculated with the same relative velocity used for the dynamic pressure, is reported above the airfoil shape. The coefficient-of-skin-friction results are shown in Fig. A2. The upper and lower surface values are plotted on the same plots, but the upper surface results have been offset halfway up the y axis for clarity. The black line that runs horizontally across the centerline of the graphs represents the value used to offset the upper surface results.

First, the inboard section of the rotor is addressed, which demonstrated nearly identical normal and chordwise force predictions across all models and RPMs. The airfoil at $r/R = 0.2$ was chosen as a representative location because it experiences the lowest-Reynolds-number flow. At this location, all of the transition models match the SA model in predicting both skin friction and pressure coefficient, which is reasonable because this section of the rotor experiences separated, turbulent flow due to its large twist. This is demonstrated by the fully turbulent skin friction predicted by all models in Figs. A2a and A2c. The coefficient of pressure is likewise identical in Figs. A1a and A1c. Therefore, ignoring 3D effects, the mean predicted values of the turbulence models show agreement at this specific flow location and condition.

However, at the $r/R = 0.9$ location, the models predict different flow states. The flow separation previously shown in Fig. A2 leads to a reduction in the mean upper surface skin friction as shown by Figs. A2b and A2d. The SA model, on the other hand, predicts higher upper surface skin friction, which is expected of a fully turbulent model. The SA model also predicts lower upper surface pressure near the leading edge in Figs. A1b and A1d, which leads to greater drag and lift. Finally, it should be noted that although the time-averaged pressure and skin friction plots shown here are quite similar, the instantaneous values are quite unsteady when using the transition models due to flow separation evident in Fig. A2.

When the distributed stresses are integrated along a rotor section, one obtains their respective contributions to the spanwise aerodynamic forces. Figure A3 shows the contribution from the tangential stress (skin friction) as a percentage of the total aerodynamic force at every spanwise section. A positive percentage indicates an increase in a value, whereas a negative percentage indicates a decrease. As expected, friction has a greater effect outboard where the flow is attached. The SA model predicts the highest friction contribution to both lift and drag overall, with similar results from the SA-MB model

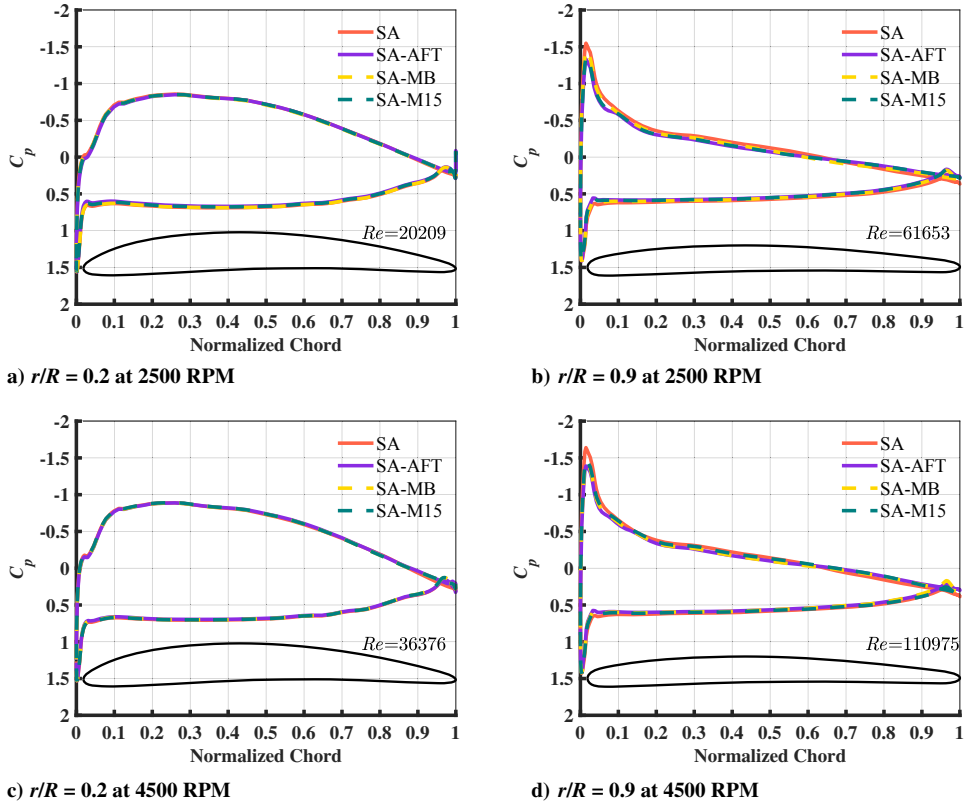

a) r/R = 0.2 at 2500 RPM

b) r/R = 0.9 at 2500 RPM

c) r/R = 0.2 at 4500 RPM

d) r/R = 0.9 at 4500 RPM

Fig. A1 Extracted coefficient of pressure versus normalized chord location at various spanwise locations for the simulated isolated T-Motor rotor in hover. The airfoil shape is superimposed, in black, at the bottom of each plot.

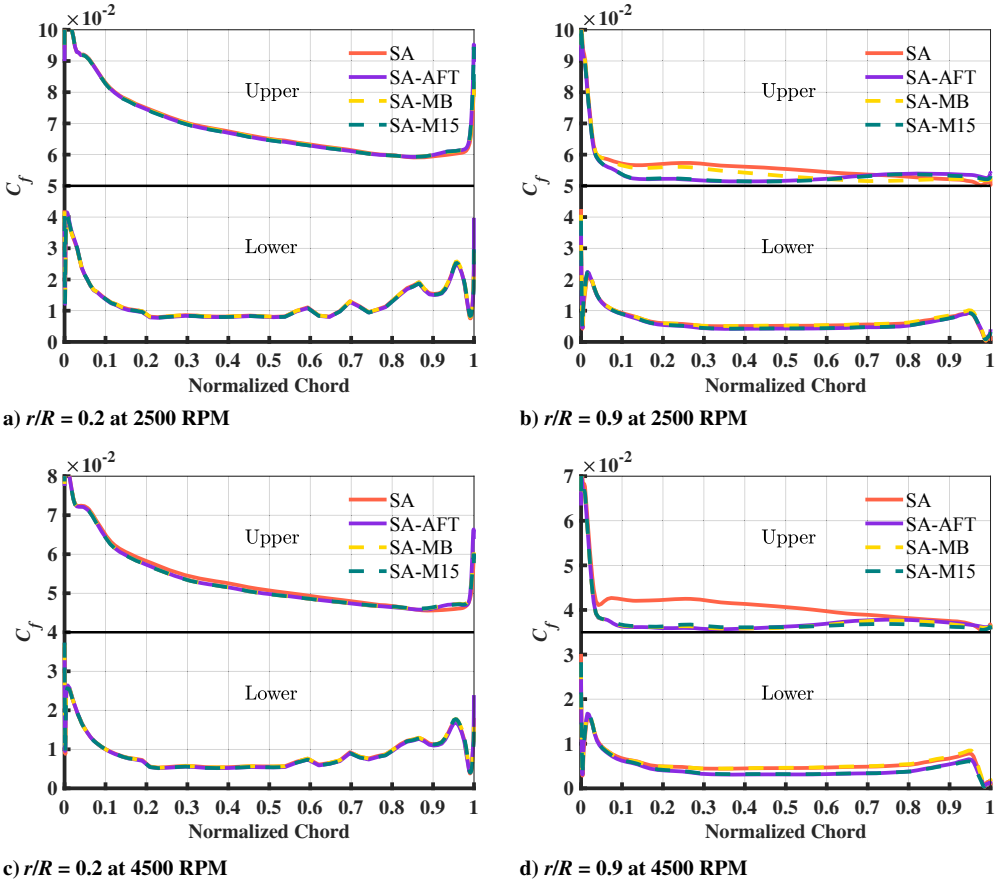

a) r/R = 0.2 at 2500 RPM

b) r/R = 0.9 at 2500 RPM

c) r/R = 0.2 at 4500 RPM

d) r/R = 0.9 at 4500 RPM

Fig. A2 Extracted coefficient of skin friction versus normalized chord location at various spanwise locations for the simulated isolated T-Motor rotor in hover. Upper surface values have been shifted halfway up the vertical axis for clarity (offset value indicated by black line).

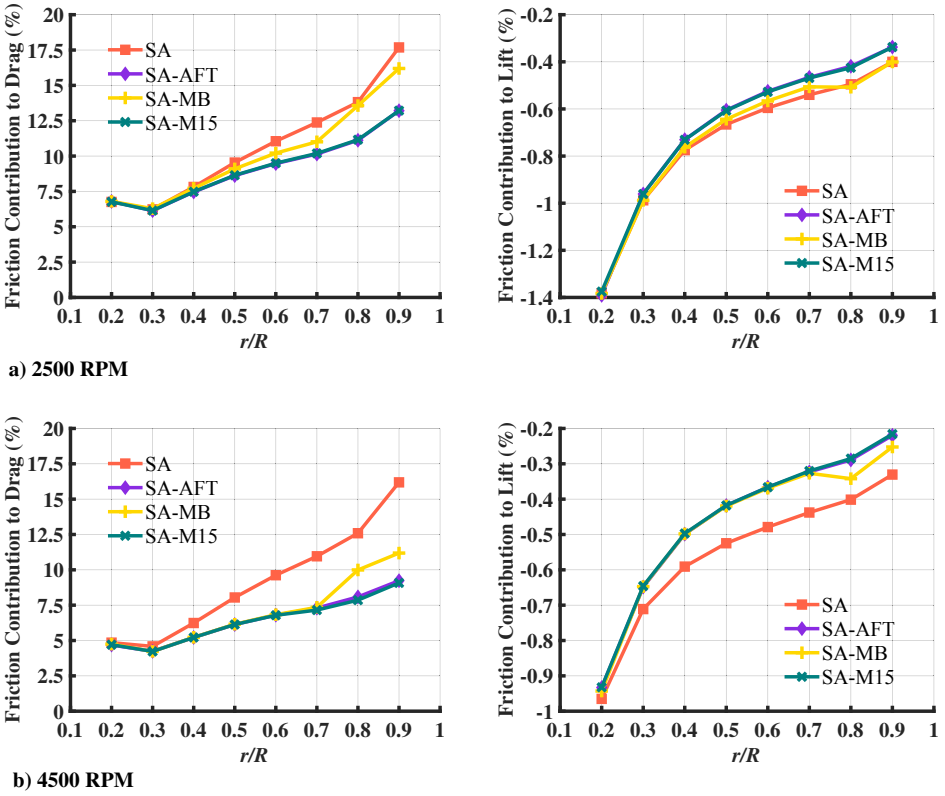

Fig. A3 Friction contribution to total drag and lift at spanwise cuts for the isolated T-Motor rotor in hover at various rotor RPMs.

at lower Reynolds numbers. As the RPM increases, the difference in the friction contribution between the models also increases, which supports the theory that the SA model's fully turbulent formulation could possibly overpredict the skin friction. Therefore, the differences in the turbulence model significantly impact both the skin friction and pressure distributions, which result in different overall aerodynamic performance predictions.

Acknowledgments

This work has been partially funded by NSF Grant 1728277. The authors would like to thank Carl Russell for providing the CAD geometry for the SUI Endurance fuselage and the T-Motor rotor blades, as well as for discussions involving the experimental conditions and laser scanning techniques. The Department of Defense High Performance Computing Modernization Program funded the first author's internships at the U.S. Army DEVCOM AvMC at NASA Ames Research Center. The authors would like to acknowledge Roger Strawn of the U.S. Army DEVCOM AvMC for providing the computing hours on the Department of Defense supercomputing clusters. The first author would like to thank Vinod Lakshminarayan, Beatrice Roget, Jay Sitaraman, Mark Potsdam, Andrew Wissink, and Steve Tran for insight into conducting Helios simulations and transition modeling. Distribution Statement A: Approved for Public Release.

References

[1] Sankaran, V., Sitaraman, J., Wissink, A., Datta, A., Jayaraman, B., Potsdam, M., Mavriplis, D., Yang, Z., O'Brien, D., Saberi, H., Cheng, R., Hariharan, N., and Strawn, R., "Application of the Helios Computational Platform to Rotorcraft Flowfields," AIAA Paper 2010-1230, Jan. 2010. https://doi.org/10.2514/6.2010-1230

[2] Sankaran, V., Wissink, A., Datta, A., Sitaraman, J., Jayaraman, B., Potsdam, M., Katz, A., Kamkar, S., Roget, B., Mavriplis, D., Saberi, H., Chen, W.-B., Johnson, W., and Strawn, R., "Overview of the Helios Version 2.0 Computational Platform for Rotorcraft Simulations," AIAA Paper 2011-1105, Jan. 2011. https://doi.org/10.2514/6.2011-1105

[3] Wissink, A., Staruk, W., Tran, S., Roget, B., Jayaraman, B., Sitaraman, J., and Lakshminarayan, V., "Overview of New Capabilities in Helios Version 9.0," AIAA Paper 2019-0839, May 2019. https://doi.org/10.2514/6.2019-0839

[4] Abras, J. N., and Hariharan, N., "Comparison of Computational Fluid Dynamics Hover Predictions on the S-76 Rotor," *Journal of Aircraft*, Vol. 55, No. 1, Jan. 2018. https://doi.org/10.2514/1.C034121

[5] Jain, R., "Sensitivity Study of High-Fidelity Hover Predictions on the Sikorsky S-76 Rotor," *Journal of Aircraft*, Vol. 55, No. 1, Jan. 2018. https://doi.org/10.2514/1.C034076

[6] Jain, R., "Hover Predictions on the S-76 Rotor with Tip Shape Variation Using Helios," *Journal of Aircraft*, Vol. 55, No. 1, Jan. 2018. https://doi.org/10.2514/1.C034075

[7] Sheng, C., Wang, J., and Zhao, Q., "Improved Rotor Hover Predictions Using Advanced Turbulence Modeling," *Journal of Aircraft*, Vol. 53, No. 5, Sept. 2016. https://doi.org/10.2514/1.C033512

[8] Richez, F., Nazarians, A., and Lienard, C., "Assessment of Laminar-Turbulent Transition Modeling Methods for Prediction of Helicopter Rotor Performance," *Proceedings of the 43rd European Rotorcraft Forum*, Milano, Italy, 2017.

[9] Sheng, C., "Role of Transition Modeling in Rotor Hover Predictions," *Journal of Aircraft*, Vol. 55, No. 1, Jan. 2018. https://doi.org/10.2514/1.C034137

[10] Govindarajan, B., and Sridharan, A., "Conceptual Sizing of Vertical Lift Package Delivery Platforms," *Journal of Aircraft*, Vol. 57, No. 6, Nov. 2020. https://doi.org/10.2514/1.C035805

[11] Barcelos, D., Kolaei, A., and Bramesfeld, G., "Aerodynamic Interactions of Quadrotor Configurations," *Journal of Aircraft*, Vol. 57, No. 6, Nov. 2020. https://doi.org/10.2514/1.C035614

[12] Han, D., and Barakos, G. N., "Aerodynamic Interference Model for Multirotors in Forward Flight," *Journal of Aircraft*, Vol. 57, No. 6, Nov. 2020. https://doi.org/10.2514/1.C035978

[13] Henricks, Q., Wang, Z., and Zhuang, M., "Small-Scale Rotor Design Variables and Their Effects on Aerodynamic and Aeroacoustic Performance of a Hovering Rotor," *Journal of Fluids Engineering*, Vol. 142, No. 8, Aug. 2020. https://doi.org/10.1115/1.4046872

[14] Thai, A. D., Jain, R., and Grace, S. M., "CFD Validation of Small Quadrotor Performance using CREATE-AV Helios," *Proceedings of the Vertical Flight Society 75th Annual Forum and Technology Display*, Paper 75-2019-0212, Philadelphia, PA, May 2019, https://vtol.org/store/product/cfd-validation-of-small-quadrotor-performance-using-create-av-helios-14483.cfm.

[15] Lakshminarayan, V. K., and Baeder, J. D., "Computational Investigation of Micro Hovering Rotor Aerodynamics," *Journal of the American Helicopter Society*, Vol. 55, No. 2, April 2010. https://doi.org/10.4050/JAHS.55.022001

[16] Diaz, P. V., and Yoon, S., "High-Fidelity Computational Aerodynamics of Multi-Rotor Unmanned Aerial Vehicles," AIAA Paper 2018-1266, Jan. 2018. https://doi.org/10.2514/6.2018-1266

[17] Hwang, J. Y., Jung, M. K., and Kwon, O. J., "Numerical Study of Aerodynamic Performance of a Multirotor Unmanned-Aerial-Vehicle Configuration," *Journal of Aircraft*, Vol. 52, No. 3, May 2015. https://doi.org/10.2514/1.C032828

[18] Misiorowski, M., Gandhi, F., and Oberai, A. A., "Computational Study on Rotor Interactional Effects for a Quadcopter in Edgewise Flight," *AIAA Journal*, Vol. 57, No. 12, Dec. 2019. https://doi.org/10.2514/1.J058369

[19] Zawodny, N. S., and Boyd, D. D., Jr., "Investigation of Rotor-Airframe Interaction Noise Associated with Small-Scale Rotary-Wing Unmanned Aircraft Systems," *Journal of the American Helicopter Society*, Vol. 65, No. 1, Jan. 2020. https://doi.org/10.4050/JAHS.65.012007

[20] Ranjan, P., Warton, W. J., and James, K. A., "A Comparison of Physics Correlation-Based Turbulence Models at Low Reynolds Numbers," *Journal of Aircraft*, Vol. 57, No. 1, Jan. 2020. https://doi.org/10.2514/1.C035588

[21] Lopes, R., Eça, L., and Vaz, G., "On the Numerical Behavior of RANS-Based Transition Models," *Journal of Fluids Engineering*, Vol. 142, No. 5, May 2020. https://doi.org/10.1115/1.4045576

[22] Yoon, S., Chaderjian, N. M., Pulliam, T. H., and Holst, T. L., "Effect of Turbulence Modeling on Hovering Rotor Flows," AIAA Paper 2015-2766, June 2015. https://doi.org/10.2514/6.2015-2766

[23] Yoon, S., Lee, H. C., and Pulliam, T. H., "Computational Analysis of Multi-Rotor Flows," AIAA Paper 2016-0812, Jan. 2016. https://doi.org/10.2514/6.2016-0812

[24] Thai, A. D., and Grace, S. M., "Prediction of Small Quadrotor Blade Induced Noise," AIAA Paper 2019-2684, May 2019. https://doi.org/10.2514/6.2019-2684

[25] Thai, A. D., Paola, E. D., Marco, A. D., Stoica, L. G., Camussi, R., Tron, R., and Grace, S. M., "Experimental and Computational Aeroacoustic Investigation of Small Rotor Interactions in Hover," *Applied Sciences*, Vol. 11, No. 21, 2021. https://doi.org/10.3390/app112110016

[26] Tran, S., Lakshminarayan, V., Sitaraman, J., and Wissink, A., "Transition Modeling in HPCMP CREATE-AV Helios v9," AIAA Paper 2019-1111, Jan. 2019. https://doi.org/10.2514/6.2019-1111

[27] Meakin, R. L., Wissink, A. M., Chan, W. M., Pandya, S. A., and Sitaraman, J., "On Strand Grids for Complex Flows," AIAA Paper 2007-3834, June 2007. https://doi.org/10.2514/6.2007-3834

[28] Wissink, A. M., Katz, A. J., Chan, W. M., and Meakin, R. L., "Validation of the Strand Grid Approach," AIAA Paper 2009-3792, June 2009. https://doi.org/10.2514/6.2009-3792

[29] Katz, A., Wissink, A., Sitaraman, J., and Sankaran, V., "Application of Strand Meshes to Complex Aerodynamic Flow Fields," *Journal of Computational Physics*, Vol. 230, No. 17, July 2011. https://doi.org/10.1016/j.jcp.2011.04.036

[30] Roget, B., Sitaraman, J., Lakshminarayan, V., and Wissink, A., "Prismatic Mesh Generation Using Minimum Distance Fields," *Computers and Fluids*, Vol. 200, March 2020. https://doi.org/10.1016/j.compfluid.2020.104429

[31] Lakshminarayan, V. K., Sitaraman, J., Roget, B., and Wissink, A. M., "Development and Validation of a Multi-Strand Solver for Complex Aerodynamic Flows," *Computers and Fluids*, Vol. 147, April 2017, pp. 41–62. https://doi.org/10.1016/j.compfluid.2017.02.002

[32] Wissink, A. M., Sitaraman, J., Jayaraman, B., Roget, B., Lakshminarayan, V. K., Potsdam, M. A., and Jain, R., "Recent Advancements in the Helios Rotorcraft Simulation Code," AIAA Paper 2016-0563, Jan. 2016. https://doi.org/10.2514/6.2016-0563

[33] Spalart, P., and Allmaras, S., "A One Equation Turbulence Model for Aerodynamic Flows," AIAA Paper 1992-0439, Jan. 1992. https://doi.org/10.2514/6.1992-439

[34] Medida, S., and Baeder, J. D., "Application of the Correlation-based Gamma-Re Theta t Transition Model to the Spalart-Allmaras Turbulence Model," *Proceedings of the 20th AIAA Computational Fluid Dynamics Conference*, AIAA Paper 2011-3979, June 2011. https://doi.org/10.2514/6.2011-3979

[35] Menter, F. R., Smirnov, P. E., Liu, T., and Avancha, R., "A One-Equation Local Correlation-Based Transition Model," *Flow, Turbulence and Combustion*, Vol. 95, No. 4, 2015, pp. 583–619. https://doi.org/10.1007/s10494-015-9622-4

[36] Coder, J. G., and Maughmer, M. D., "Computational Fluid Dynamics Compatible Transition Modeling Using an Amplification Factor Transport Equation," *AIAA Journal*, Vol. 52, No. 11, 2014, pp. 2506–2512. https://doi.org/10.2514/1.J052905

[37] Coder, J. G., "Enhancement of the Amplification Factor Transport Transition Modeling Framework," AIAA Paper 2017-1709, Jan. 2017. https://doi.org/10.2514/6.2017-1709

[38] Coder, J., Pulliam, T. H., and Jensen, J. C., "Contributions to HiLiftPW-3 Using Structured, Overset Grid Methods," AIAA Paper 2018-1039, Jan. 2018. https://doi.org/10.2514/6.2018-1039

[39] Langtry, R. B., and Menter, F. R., "Correlation-Based Transition Modeling for Unstructured Parallelized Computational Fluid Dynamics Codes," *AIAA Journal*, Vol. 47, No. 12, Dec. 2009, pp. 2894–2906. https://doi.org/10.2514/1.42362

[40] Russell, C., Jung, J., Willink, G., and Glasner, B., "Wind Tunnel and Hover Performance Test Results for Multicopter UAS Vehicles," *Proceedings of the American Helicopter Society 72nd Annual Forum*, West Palm Beach, FL, May 2016, Paper 72-2016-374.

[41] Russell, C., Willink, G., Theodore, C., Jung, J., and Glasner, B., "Wind Tunnel and Hover Performance Test Results for Multicopter UAS Vehicles," NASA TM-2018-219758, 2018.

[42] Kamkar, S., Wissink, A., Sankaran, V., and Jameson, A., "Feature-Driven Cartesian Adaptive Mesh Refinement for Vortex-Dominated Flows," *Journal of Computational Physics*, Vol. 230, No. 16, July 2011, pp. 6271–6298. https://doi.org/10.1016/j.jcp.2011.04.024

[43] Lakshminarayan, V., Sitaraman, J., and Wissink, A., "Sensitivity of Rotorcraft Hover Predictions to Mesh Resolution in Strand Grid Framework," *AIAA Journal*, Vol. 57, No. 8, Aug. 2019. https://doi.org/10.2514/1.J056571

[44] Roache, P. J., "Perspective: A Method for Uniform Reporting on Grid Convergence Studies," *Journal of Fluids Engineering*, Vol. 116, No. 3, Sept. 1994, pp. 405–413. https://doi.org/10.1115/1.2910291

[45] Wolf, C. C., Schwarz, C., Kaufmann, K., Gardner, A. D., Bosbach, D. M. J., Scahnz, D., and Schröder, A., "Experimental Study of Secondary Vortex Structures in a Rotor Wake," *Experiments in Fluids*, Vol. 60, Oct. 2019. https://doi.org/10.1007/s00348-019-2807-1

[46] Abras, J., Narducci, R., and Hariharan, N., "Wake Breakdown of High-Fidelity Simulations of a Rotor in Hover," AIAA Paper 2019-0593, Jan. 2019. https://doi.org/10.2514/6.2019-0593

[47] Abras, J., Narducci, R., and Hariharan, N., "Impact of High-fidelity Simulation Variations on Wake Breakdown of a Rotor in Hover," AIAA Paper 2020-0531, Jan. 2020. https://doi.org/10.2514/6.2020-0531

[48] Hariharan, N., Abras, J., and Narducci, R., "An Overview of Wake Breakdown in High-Fidelity Simulations of Rotor-in-Hover," *Proceedings of the 76th Vertical Flight Society Annual Forum*, Virtual, Paper 76-2020-0316, Oct. 2020, https://vtol.org/store/product/an-overview-of-wake-breakdown-in-highfidelity-simulations-of-rotorinhover-16473.cfm.

[49] Bodling, A., and Potsdam, M., "Numerical Investigation of Secondary Vortex Structures in a Rotor Wake," *Proceedings of the Vertical Flight Society 76th Annual Forum*, Paper 76-2020-0341, Virtual, Oct. 2020, https://vtol.org/store/product/numerical-investigation-of-secondary-vortex-structures-in-a-rotor-wake-16475.cfm.

[50] Russell, C., and Sekula, M., "Comprehensive Analysis Modeling of Small-Scale UAS Rotors," *Proceedings of the American Helicopter Society 73rd Annual Forum*, Paper 73-2017-0096, Fort Worth, TX, May 2017.

[51] Leishman, G., *Principles of Helicopter Aerodynamics*, 2nd ed., Cambridge Univ. Press, New York, 2006, Chap. 2.

[52] Jia, Z., and Lee, S., "Impulsive Loading Noise of Lift-Offset Coaxial Rotor in High-Speed Forward Flight," *AIAA Journal*, Vol. 58, No. 2, Feb. 2020. https://doi.org/10.2514/1.J058295